LATVIAN JOURNAL of PHYSICS and TECHNICAL SCIENCES

ISSN 0868 - 8257

3

(Vol. 55)

2018

SATURS

CONTENTS

СОДЕРЖАНИЕ

LATVIAN JOURNAL of PHYSICS and TECHNICAL SCIENCES

LATVIJAS FIZIKAS un TEHNISKO ZINĀTŅU ŽURNĀLS

ЛАТВИЙСКИЙ ФИЗИКО-ТЕХНИЧЕСКИЙ ЖУРНАЛ

Published six times a year since February 1964
Iznāk sešas reizes gadā kopš 1964. gada februāra
Выходит шесть раз в год с февраля 1964 года

3 (Vol. 55) • 2018

RĪGA

INDEKSĒTS (PUBLICĒTS) | INDEXED (PUBLISHED) IN

www.scopus.com
www.degruyter.com
EBSCO (Academic Search Complete, www.epnet.com), INSPEC (www.iee.org.com). VINITI (www.viniti.ru), Begell House Inc/ (EDC, www.edata-center.com).

Izdevējs: Fizikālās enerģētikas institūts
Reģistrācijas apliecība Nr. 0221
Redakcija: Krīvu iela 11, Rīga, LV-1006
Tel. 67551732, 67558694
e-pasts: ezerniec@edi.lv
Interneta adrese: www.fei-web.lv

sciendo

LATVIAN JOURNAL OF PHYSICS
AND TECHNICAL SCIENCES
2018, N 3

DOI: 10.2478/lpts-2018-0016

PHYSICAL AND TECHNICAL ENERGY PROBLEMS

EFFECTIVENESS OF THE TOOTH ZONE OF INDUCTOR ELECTRIC MACHINE

A. Serebryakov, E. Kamolins, K. Gulbis, K. Sejejs

Riga Technical University
12/1 Azenes Str., Riga, LV-1048, LATVIA
e-mail: edmunds.kamolins@rtu.lv

The authors consider several tens of rotor tooth and slot profiles for the inductor electric machine in order to gain the maximum EMF of the armature winding at the minimum of highest harmonics, owing to which the specific power and efficiency of the machine can be raised.

The research considers usage of analytical methodology and finite element method (FEM), where the latter includes magnetic saturation and actual magnetic field line distribution.

The main data of both calculations are summarised in the results of the study. From the obtained results, it can be concluded that, in most cases, the analytical method is not applicable to the qualitative determination of the highest harmonic content of the EMF, since the plane of the magnetic field lines does not close in parallel and their distribution is directly related to the configuration of the teeth zone.

The possibility of using the inductor generators for direct connection to the grid is demonstrated in the study.

Keywords: *harmonic distortion, inductor electric machine, tooth shapes*

1. INTRODUCTION

The inductor electric machines (IEMs) – owing to their simple and reliable design – have received wide recognition in technology – mainly as machines of low and intermediate power (i.e., diesel generators, train car and welding generators, gearless wind generators, phase splitters, etc.). A majority of such machines supply load via an intermediate converter (rectifier, frequency converter, etc.). The main criterion of their operational quality is the value of the armature winding EMF, while the EMF sinusoidal shape, which is determined by the highest harmonic content, serves as a supplementary criterion.

Serviceability of an IEM is determined by the permeance value and the rate of its changing in the airgap between the teeth of stator and rotor at running of the latter. The value of permeance depends on the variation of the airgap between these teeth, while its rate – on the rotational speed of the rotor. In this process, the magnetic flux through the airgap and the magnetic-flux linkage of the armature winding are changing; as a result, the EMF induced there affects the machine power.

In IEMs of the known design, the magnetic flux pulsating from its maximum value to the minimum one also contains – apart from a variable component that determines EMF – a constant component of its Fourier-series expansion; this component does not create EMF, loads the magnetic core by raising its weight, increases the inductance of the armature winding and its inductive reactance and decreases the machine power. Therefore, a decrease in the constant component of magnetic flux can serve as a supplementary criterion of the IEM operational efficiency.

To raise the extent of using the magnetic flux in an IEM is the problem of basic importance. It is desirable that there is such a change in the tooth zone permeance (being in essence the permeance of its airgap), and, respectively, the armature winding magnetic-flux linkage that would provide the maximum first harmonic component, which determines the main EMF as well as the minimum zeroth component and the highest harmonic components.

Investigations in this direction (e.g., [1]–[3]) have embraced some part of possible shapes of rotor teeth – mainly a trapezoidal with curvatures in slots and a rectangular one. It is important to look at more recent investigation to different types of machines where possible shapes of rotor teeth are evaluated (e.g., [4]–[6]). Investigations have been carried out both analytically and by modelling. A major portion of possible tooth profiles have not been elucidated. Therefore, the present research gives determination of the harmonic series for the permeance of the IEM tooth zone airgap in order to widen the composition of rotor tooth profiles and their corresponding geometric parameters. Based on these considerations, the research provides estimation of the values and forms of armature winding EMF.

This investigation relates to the IEMs with rotor teeth evenly arranged along a recess.

2. PROFILES OF ROTOR TEETH AND THEIR PARAMETERS

By the character of airgap variations in the tooth zone along the recess the IEMs can be divided into two groups: whose zones have a section of rotor tooth pitch with a constant gap, and whose zones are without such a pitch – that is, their airgap is variable along the rotor tooth pitch. To the first group we can relate the IEMs having rectangular rotor teeth with parallel walls (Fig. 1, a), trapezoidal ones (Fig. 1, b), rectangular with curvatures (Fig. 1, c), of combined shape (Fig. 1, d) with the airgap uniform at the middle section, but at tooth edges changing in compliance with the cosecant law [7], [8]:

$$\delta = \delta_{\min} \cdot \csc(b_R^{\circ}) = \frac{\delta_{\min}}{\sin(b_R^{\circ})}. \qquad (1)$$

Profiles of the 2nd group are considered in Section 5. The rectangular profile is most often encountered.

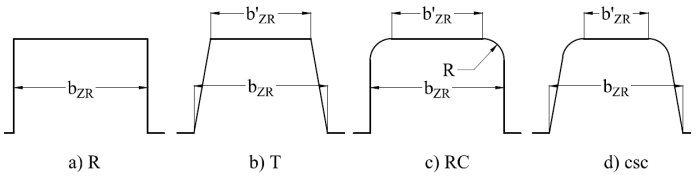

Fig. 1. Rotor tooth shapes with constant air gap.

Figure 2 shows a fragment (a) and a developed (b) view of a tooth zone with a rectangular tooth; geometric parameters indicated are the following:

a) D_S, D_R, D_P – the diameter of stator, rotor and circumference across the rotor slot bottom;

b) b_S (b_R), b_{ZS} (b_{ZR}), b_{PS} (b_{PR}) – the tooth pitch, the width of tooth (Z), the width of slot (P), for stator (S) and rotor (R);

c) b_S° (b_R°), b_{ZS}° (b_{ZR}°), b_{PS}° (b_{PR}°), b_S^E (b_R^E), b_{ZS}^E (b_{ZR}^E), b_{PS}^E (b_{PR}^E) – similar angular sizes in degrees ($^\circ$) and electrical degrees (E);

d) h_{ZR} – the rotor tooth height;

e) $\delta_{\min}$, $\delta_{\max}$ – the minimum and maximum airgaps.

The parameters indicated above are determined by the formulas:

$$b_S = \frac{\pi D_S}{Z_S}; \qquad b_R = \frac{\pi D_R}{Z_R}; \qquad b_S^\circ = \frac{360^\circ}{Z_S}; \qquad b_R^\circ = \frac{360^\circ}{Z_R};$$

$$b_{ZS}^E = \frac{360^\circ b_{ZS}}{b_R}; \qquad b_{ZR}^E = \frac{360^\circ b_{ZR}}{b_R}; \qquad b_{PR}^E = b_R^E - b_{ZR}^E, \tag{2}$$

where Z_S and Z_R are the numbers of stator and rotor teeth.

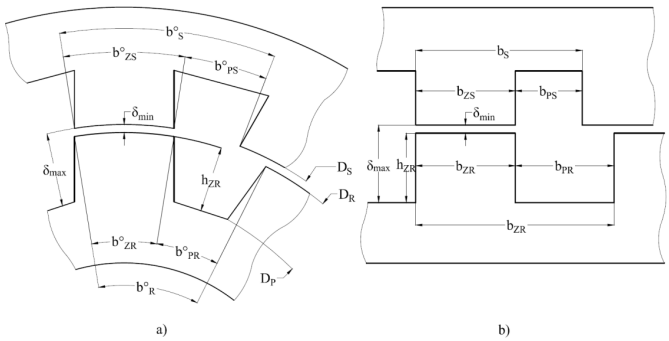

Fig. 2. Tooth zone with a rectangular tooth fragment (a) and a developed view (b).

At investigation of tooth zones, the parameters b_{ZS} (c) and b_{ZR} (b_{ZR}°) are to be varied in order to achieve the optimal result. It is more convenient to deal with the

parameters expressed via the relation to the rotor tooth pitch b_R, e.g., $b_{ZS}/b_R = 0.4$; $b_{ZR}/b_R = 0.5$. Having omitted the designations in letters, a tooth zone might be conditionally designated as a sequence of cipher values (through a hyphen) of the mentioned relationships (for example, 0.4–0.5), with adding the designation of the tooth profile shape: R – rectangular; T – trapezoidal, RC – rectangular with curvature; K – cosecant, etc. For zones T, RC, and K between the b_{ZS}/b_R; b_{ZR}/b_R values it is necessary to add the ratio of width b'_{ZR} of the section with a uniform airgap (Fig. 1, b, c, d) to k, b_R, B. In such cases, the conditional designation cipher of the tooth zone will be: 0.4–0.3–0.5*RC*, i.e., $b_{ZS}/b_R = 0.4$; $b'_{ZR}/b_R = 0.3$; $b_{ZR}/b_R = 0.5$; the profile is rectangular with curvatures. All the mentioned aspects also relate to the corresponding angular sizes. Thus, zone 0.3–0.5 R has $b^E_{ZS} = 0.3 \cdot b^E_R = 0.3 \cdot 360^\circ = 108^\circ$; $b^E_{ZR} = 0.5 \cdot b^E_R = 0.5 \cdot 360 = \ = 180^\circ$; the tooth is rectangular.

The most general – that is, suitable for the majority of IEMs of diversified specification – optimal tooth zone parameters according to recommendations [1]–[3], [9]–[12] are:

$$b_{ZS}(b_{ZR}) = (0.3 \div 0.4) b_S (b_R);\ b_{PR} = \left(\frac{2}{3} \div \frac{3}{5}\right) b_R;$$
$$h_{ZR} \le 0.75 b_{PR};\ \delta = \left(\frac{1}{200} \div \frac{1}{300}\right) D_R \qquad (3)$$

The increase in $b^E_{ZS} > 0.5 b_S$ is connected with the decrease in the width of slot for winding, the increase in the diameter of stator and the weight of machine. The decrease in the b_{ZR} as compared with b_{ZS} results in a decreasing permeance of the tooth zone and its effectiveness.

To ensure the identity of the investigation into tooth zones with different rotor tooth and slot profiles, a number of parameters should remain invariable; this refers to b_R; b_S; h_{ZR}; δ; D_S; D_R as well as to the number of stator and rotor teeth, Z_S and Z_R.

3. THEORETICAL PREREQUISITES OF THE INVESTIGATION

In the inductor machine at the displacement of a rotor tooth relative to a stator tooth, the permeance of airgap under the stator tooth changes, and, consequently, the magnetic flux and magnetic-flux linkage with the armature winding are also changing, and there is induced EMF with a period $T = 2\pi$ rad. (or 360° el.). This means that the rotor tooth plays the role of a pole pair "p" of a common synchronous machine, i.e., in the IEM we will have $p = Z_R$ with the EMF frequency $f = \frac{Z_R n}{60}$ where n - is the rotational speed, min^{-1}.

In order to achieve that in the tooth zone on the rotor tooth pitch b_R (b°_R) mutual overlapping would not occur by the rotor tooth of more than (even if partially) one stator tooth, the following condition must be fulfilled:

$$b_{ZS} + b_{ZR} \le b_R;\ b^\circ_{ZS} + b^\circ_{ZR} \le b^\circ_R;\ b^E_{ZS} + b^E_{ZR} \le b^E_R. \qquad (4)$$

As this takes place, for each pass of a rotor tooth relative to a stator tooth the required angle of rotor turning α° is determined by parameters b°_{ZS}; b°_{ZR}; $(b^{E}_{ZS}; b^{E}_{ZR})$ and is equal to their sum, i.e.:

$$\alpha^{\circ} = b^{\circ}_{ZS} + b^{\circ}_{ZR};\ \alpha^{E} = b^{E}_{ZS} + b^{E}_{ZR}. \tag{5}$$

The sum $b^{\circ}_{ZS} + b^{\circ}_{ZR}$, which at mutual displacement of the rotor tooth relative to the stator tooth provides inducing the EMF with a period $T = 360^{\circ}$, in the electrical designation is equivalent to $360°$. Thus, in electrical units $\alpha^{E} = \alpha^{\circ} Z_R = 360^{\circ} = 2\pi$.

Conditions (2) might be expressed in the form:

$$\frac{b^{\circ}_{ZS}}{b^{\circ}_{R}} + \frac{b^{\circ}_{ZR}}{b^{\circ}_{R}} \le 1;\ \frac{b^{E}_{ZS}}{b^{E}_{R}} + \frac{b^{E}_{ZR}}{b^{E}_{R}} \le 1. \tag{6}$$

Conditions (2)–(5) determine possible combinations of parameters $b_{ZS} - b_{ZR}$; $b^{\circ}_{ZS} - b^{\circ}_{ZR}$; $b^{E}_{ZS} - b^{E}_{ZR}$. Here a set of such variants can be composed, which in a designing point of view are executable both at $b_{ZS} \le b_{ZR}$ and at $b_{ZS} \ge b_{ZR}$.

For the investigation purposes, having established a gradation of variations in the indicated sizes as $0.1b_R$ $(0.1b^{E}_{R})$, it is possible to restrict ourselves to the finite number of variants.

Thus, at $\frac{b_{ZS}}{b_R} = 0.3$ the variants $\frac{b_{ZR}}{b_R}$ will be: 0.3; 0.4; 0.5; 0.6; 0.7; (7)

At $\frac{b_{ZS}}{b_R} = 0.4$ these variants will be: 0.3; 0.4; 0.5; 0.6;

At $\frac{b_{ZS}}{b_R} = 0.5$ these variant will be: 0.5.

This means that at its known (selected, calculated) value, b_{ZS} (b^{E}_{ZS}) determines the variant of combination b_{RS} (b^{E}_{RS}) as $b_{ZR} \le b_R - b_{ZS}$ or $b^{E}_{ZR} \le b^{E}_{R} - b^{E}_{ZS}$ shown in (7).

During the period corresponding to the sum $b^{E}_{ZS} + b^{E}_{ZR}$ displacement occurs of a rotor tooth relative to a stator tooth as well as relevant variations in the air-gap permeance, flux, magnetic-flux linkage with the armature winding and in the induced there EMF. Therefore, this period and the corresponding angle γ^{E}_{P} could be conditionally named "operational", while from expression (4) it follows that $\gamma^{E}_{P} = b^{E}_{ZS} + b^{E}_{ZR}$.

In passing of a rotor slot relative to a stator tooth, changes mentioned above and inducing EMF do not practically occur; therefore, this time interval and the relevant angle γ^{E}_{x} can be conditionally named "idle run" while $\gamma^{E}_{x} = b^{E}_{R} - \gamma^{E}_{P}$. The greater the working time is, the higher the efficiency of IEM operation. The maximum efficiency will be at $\gamma^{E}_{x} = 0$ and $b^{E}_{ZS} = b^{E}_{ZR} = 180^{\circ}$ which corresponds to the zone 0.5–0.5. However, these assumptions need verification.

The airgap between stator and rotor in the rotor tooth pitch b_R (b_R^E) along D_S is determined by the tooth and slot profiles, and in the range of the profiles under consideration (7) is not unambiguous. Thus, even in the simplest by configuration profile of rotor tooth, i.e., rectangular with the associated trapezoidal slot (Fig. 1, a) the airgap is varying from the minimum $\delta_{\min}$ in b_{ZR} limits up to the maximum $\delta_{\max}$ in b_{PR} limiting values, and differs for different b_R (b_R^E) values. This presents definite difficulties at establishment of the rule of airgap permeance variations, which would allow for its determination in any point of a tooth pitch b_R (b_R^E).

It would be worthwhile to replace the line of investigation into the tooth and slot profiles by a step-wise one, having broken up these profiles in the tooth pitch into a series of equal by width (angle) elementary sections Δb_R (Δb_R^E) (Fig. 2). The height of the elementary section between the line of D_S and the line of profiles will appear as the airgap value for this section. In this case, either Δb_R or $\left(\Delta b_R^E\right)$ value is selected and the number χ of elementary sections is determined:

$$\chi = \frac{b_R}{\Delta b_R} = \frac{\pi D_R}{Z_R \Delta b_R};\ \chi = \frac{b_R^E}{\Delta b_R^E} = \frac{360^\circ}{\Delta b_R^E}. \tag{8}$$

Vice versa, with the number χ defined, the values $\Delta b_R, \Delta b_R^\circ, \Delta b_R^E$ are determined (the last one in el. degrees). To all the sections index numbers are assigned: $i = 1, 2, 3, ..., \chi$ the corresponding airgaps will be numbered similarly δ_i. The specific airgap permeance corresponding to the i-th section Δb_{Ri} (Δb_{Ri}^E) can be determined as in [8]:

$$\lambda_i = \frac{S_i \mu_0}{\delta_i} = \frac{\Delta b_{Ri} l \mu_0}{\delta_i}, \tag{9}$$

where S_i; Δb_{Ri}; l are the aria, width, and axial length of elementary section, μ_0 is the magnetic permeability of vacuum.

When using formula (9) it is necessary to meet the following conditions:

$\frac{\delta_i}{\Delta b_{Ri}} \le 0.04$; $\frac{\delta_i}{l} \le 0.04$, which would ensure the error not greater than 10 %.

Since S_i, Δb_{Ri}, l, μ_0 are constant values and do not depend on whether or not the rotor is running, assuming the product $\Delta b_{Ri} l \mu_0$ to be equal to an arbitrary unit, we will obtain the expression for specific permeance of the elementary profile section in arbitrary units of magnetic permeance in the form:

$$\lambda_i = \frac{1}{\delta_i}, \tag{10}$$

where the δ_i value can be determined from the sketch of developed view of the machine tooth zone (Fig. 2) or, otherwise, calculated.

The magnetic flux through the elementary section square S_i is $\Phi_i = F \cdot \lambda_i$,

and at choosing the MMF of F excitation equal to the MMF arbitrary unit ($F=1$) the flux can be determined in the arbitrary units for flux as $\Phi_i = \lambda_i$.

The magnetic induction in the elementary section is $B_i = \dfrac{\Phi_i}{S_i}$ and, since $S_i = const.$, then, having assumed S_i as being equal to one arbitrary unit for square, we will obtain this induction in arbitrary units for induction, i.e., $B_i = \lambda_i$.

The magnetic-flux linkage Ψ_i of the armature winding coil due to the elementary section flux is $\Psi_i = \Phi_i \cdot W_C$ taking the number of coil turns W_C equal to one arbitrary unit for turns, we can consider Ψ_i in arbitrary units for magnetic-flux linkage, i.e., $\Psi_i = \lambda_i$.

4. ANALYSIS OF THE ROTOR TOOTH SHAPES

All the aspects highlighted above determine the methods for investigation that can be used at definite values of the input parameters $D_S, D_R, D_P, b_R\left(b_R^o, b_E^o\right)$, $b_{ZS}^o, b_{ZR}^o, h_{ZR}, \delta_{\min}$, as well as Z_R and Z_S that are chosen or calculated preliminarily.

For example, EMF e_1 of the first harmonic component of magnetic-flux linkage $\Psi_1 = a_1 \cos\alpha^E$ will be determined as

$$e_1 = -\frac{d\Psi_1}{dt} = -\frac{d}{dt}\left(a_1 \cos\alpha^E\right) = -\frac{d}{dt}\left(a_1 \cos\omega Z_R t\right) = a_1 \omega Z_R \sin\alpha^E \qquad (12)$$

The EMFs of other harmonic components of magnetic-flux linkage are determined similarly; thus, in general form the expression for machine EMF will be:

$$e(\alpha^E) = \pm a_1 \sin\alpha^E \pm 2a_2 \sin 2\alpha^E \pm ... \pm k a_k \sin k\alpha^E = \sum_{k=1}^{n} k a_k \sin(k\alpha^E), \qquad (13)$$

where k is the EMF harmonic component number (k=1,2,3,...).

By using the investigation algorithm that would be inverse of the considered in Section 3, it is possible – assuming the $\Psi(\omega t)$ variations – to carry out synthesis of tooth and slot profiles.

To compare analytically obtained results, where most calculations are done according to [13], [14] recommendations, the FEA simulations are done using computer software Flux 2D by Cedrat Reaserch [15]. FEA method is well established and in-depth description is available in many sources. In contrast to analytical method, FEA method takes into account magnetic saturation. Magnetic saturation has profound influence on armature EMF sinusodiallity [6], [16].

The whole node number of the model under investigation is about 10000. The simulation is carried out as magneto-static application where movement of rotor by angle α is imposed for full pole pitch $b_R^E = 360^\circ$ el. Calculation step is chosen as $\Delta\alpha^E = 0.5^\circ$. In contrast to the analytical method, the geometry of model is defined in metric units. Magnetizing force is defined to such a value that yields saturation of iron core just below a saturation point. Figure 3 shows the results obtained for magnetic field density in T.

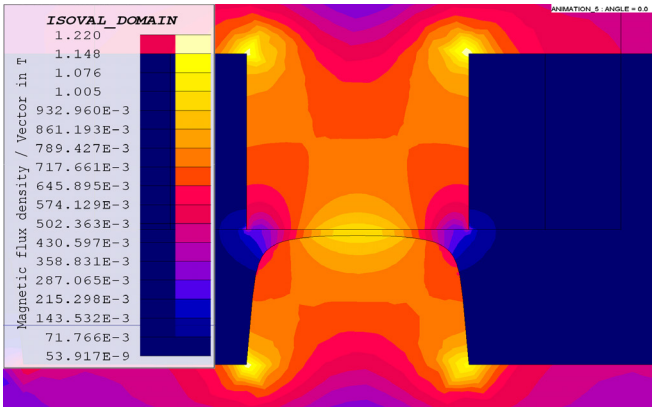

Fig. 3. Magnetic field density for $0.5-0.5\csc(b_R^\circ)$ at $\alpha^E = 180^\circ$.

Through FEA studies, using in software built-in tools, alternating flux linked with the winding can be obtained. EMF induced in coil can be found by derivative of alternating flux over time $EMF = -W_C \dfrac{d\Phi}{dt}$, where turn number $W_C = 1$ is assumed. Machine rotation speed is not defined within the framework of research, therefore derivative over angle α^E is used $\dfrac{d\Phi}{d\alpha^E}$ in $\dfrac{Wb}{\deg}$ with respect to $EMF = K\dfrac{d\Phi}{d\alpha^E}$, where K – the coefficient describing relationship between machine rotation speed and angle α^E. Previous research shows applicability of FEA method to EMF harmonic content analysis [16].

5. TOOTH ZONES WITH NONUNIFORM AIRGAP

Figure 4 gives fragments of tooth zones with nonuniform airgap on the rotor tooth pitch: (a) – a tooth zone 0.5–0.5*K1*, with the airgap spread along the rotor tooth width as $\delta = \delta_{\min} \cdot \csc(b_R^\circ)$, $\delta_{\min} = 1$, $h_{ZR} = 22$, $\delta_{\max} = 23$; (b) – a tooth zone 0.5–0.5*S*, with the airgap spread along as $\delta = 2 - \sin(b_R^\circ)$, $\delta_{\min} = 1$, $h_{ZR} = 22$, $\delta_{\max} = 2$; (c) Fig. 4,c – a tooth zone 0.5–0.5*K* with the tooth of wedge shape, $\delta_{\min} = 1$, $\delta_{\max} = 1.5$.

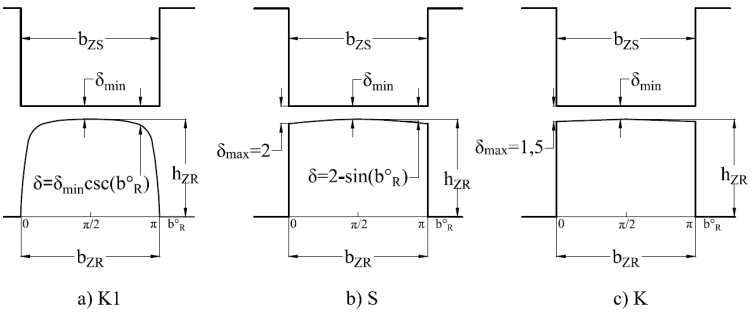

Fig. 4. Fragments of rotor tooth zones with nonuniform airgap.

The results of investigation into such tooth zones are presented in Table 1. As criteria of IEM efficiency at its operation with one or other rotor tooth profile given in Table 1 the following ones are used: $\frac{E_1}{E}\%$ – the ratio of operating EMFs of the first harmonic E_1 to the overall EMF of armature winding E expressed in percent;

$\frac{E_i}{E}\%$ – the ratio of operating highest EMF harmonics E_i to the overall EMF of armature winding E expressed in percent, where $i = 2,3,...,5$;

$THD = \frac{\sqrt{\sum_{i=2}^{15} E_i^2}}{E_1}$ – the total harmonic distortion (THD), where first 15 harmonics are taken into account, to the first harmonic E_1 expressed in percent.

In the graphic form the results of investigation are presented in Fig. 7. If we compare the factors pointing to the influence exerted by rotor tooth profiles on the value and shape of the armature winding EMF reported in [1]–[3]with those obtained in the given investigation, it could be seen that the results are practically identical for the profiles considered in the mentioned sources, and can therefore serve as a criterion of confidence in the results of our investigation into the whole set of rotor tooth profiles using the methods proposed in the present research.

6. ANALYTICAL TREATMENT OF THE INVESTIGATION RESULTS FOR THE IEM TOOTH ZONES

Based on the results of investigation into the IEM tooth zones, the following conclusions can be drawn:

1) Tooth zones with unequal values b_{ZS}^E and b_{ZR}^E (e.g. 0.4–0.5T) – when the conditions $b_{ZS}^E + b_{ZR}^E \le b_R^E$ are observed – have on the corresponding graphs $\Psi(\alpha^E)$ (Fig. 5) the sections (shelves) with constant magnetic-flux linkage, in the range of whose values α^E no EMF in the armature winding is induced, this reduces the overall winding EMF and the effectiveness of using such "asymmetrical" tooth zones.

2) The mentioned circumstance is a validation of presumption that has been considered in Section 2 as to the negative influence on the effectiveness of a tooth zone exerted by its "idle run" $\gamma_x^E = \gamma^E - (b_{ZS}^E + b_{ZR}^E)$ – the greater the γ_x^E, the lower the EMF value for the given group of tooth zones (Fig. 5).

3) Similar effect is also observed for tooth zones with equal b_{ZS}^E; b_{ZR}^E values, e.g., 0.3–0.3R and 0.4–0.4R. This effect manifests itself in a decreased amplitude on the corresponding graph $\Psi(\alpha^E)$ and in a decreased induced EMF (Fig. 5).

4) The highest in effectiveness EMF is for the tooth zone 0.5–0.5R in which the "idle run" $\gamma_x^E = 0$ is theoretically absent, so the whole time of rotor tooth passing under stator tooth is operating $\gamma_P^E = (b_{ZS}^E + b_{ZR}^E)$; this circumstance validates the presumption about the highest in effectiveness EMF for the tooth zone with $b_{ZS}^E = b_{ZR}^E = 180^\circ$.

5) By analytical calculations the minimum content of the highest harmonic EMFs is provided by the tooth zone $0.5 - 0.5\csc(b_R^\circ)$ (Table 1), in which the uneven

airgap on the b_R° rotor pitch is spread by the cosec law (3) in the range $b_R^\circ = 0 \div 180^\circ$. A machine with such a tooth zone has the EMF shape close to sinusoid (Fig. 7).

6) By FEA calculations the minimum content of the highest harmonic EMFs is provided by the tooth zone $0.5 - 0.5\sin(b_R^\circ)$ (Table 1). A machine with such a tooth zone has the EMF shape close to sinusoid (Fig. 7).

7) As a consequence, the generators made based on the use of tooth zone $0.5 - 0.5\sin(b_R^\circ)$ fulfil EN 50160 standard [17] criteria on most terms and with minor improvements may be applied for direct connection to the grid, without using additional intermediate convertors (Table 1).

8) Difference between analytical calculations and FEA calculations (Fig. 6) are due to magnetic steel saturation (Fig. 4) and assumed simplifications for analytical calculations. The magnetic field lines are bent in the air gap as shown in Fig. 8, where analytical calculations do not take this effect into account. For conventional electrical machine design, coefficients are used to take this effect into account.

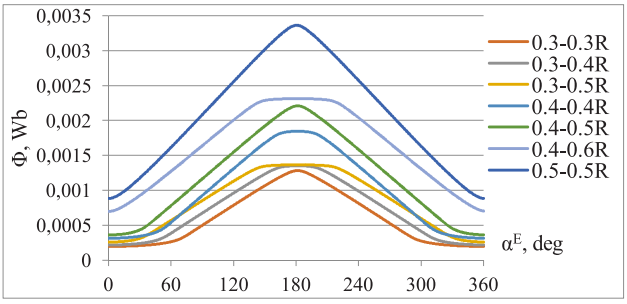

Fig. 5. Magnetic flux for rectangular shaped teeth.

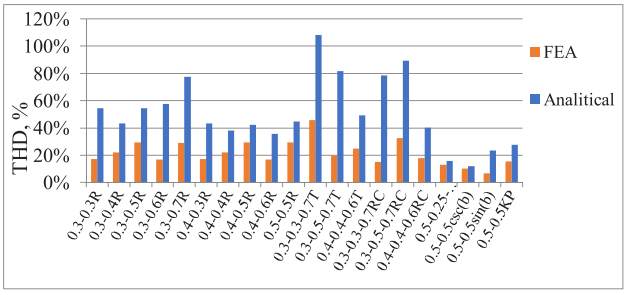

Fig. 6. EMF total harmonic distortion for analytically calculated and finite element results.

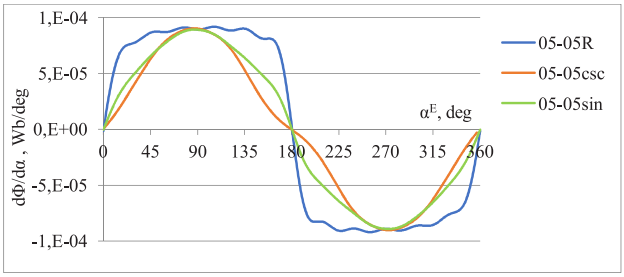

Fig. 7. $\frac{d\Phi}{d\alpha}$ shape that indicates EMF shape.

Table 1

EMF Harmonic Content Data for Chosen Rotor Tooth Profiles

Tooth profile	Analytical	FEA	E_1/E, %	$\frac{d\Phi}{d\alpha}$, Wb/deg	Harmonic content to fundamental			
	THD, %	*THD*, %			E_2, %	E_3, %	E_4, %	E_5, %
0.5–0.5*R*	44.0 %	29.6 %	95.8 %	$7.76 \cdot 10^{-5}$	2.55 %	25.40 %	1.68 %	11.92 %
0.5-0.5*csc* (b_R°)	11.9 %	10.2 %	99.5 %	$6.06 \cdot 10^{-5}$	5.70 %	7.64 %	1.77 %	3.02 %
0.5–0.5*sin*(b_R°)	23.4 %	6.9 %	99.7 %	$6.44 \cdot 10^{-5}$	0.28 %	4.97 %	1.15 %	4.11 %
EN 50160	8 %	8 %	-	-	2 %	5 %	1 %	6 %

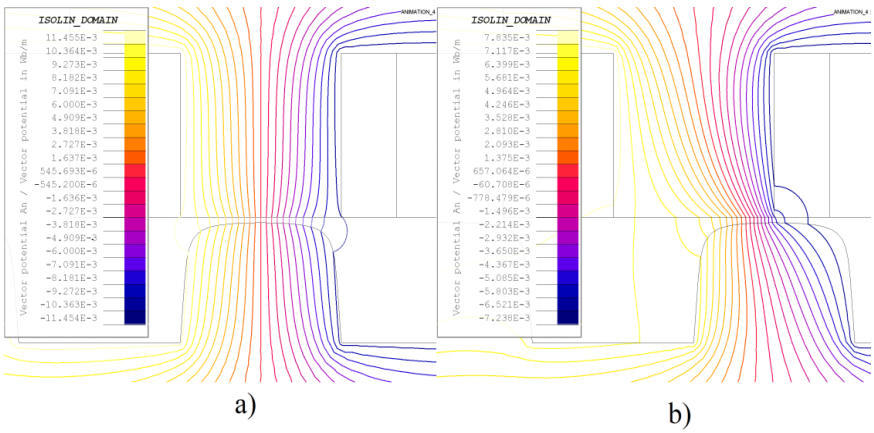

Fig. 8. Magnetic field vector potential for $0.5 - 0.5\csc(b_R^\circ)$ (a) $\alpha^E = 180^\circ$ (b) $\alpha^E = 270^\circ$.

7. CONCLUSIONS

Depending on the configuration of rotor teeth and slots and the relationships between their geometric parameters more than 20 types of IEM tooth zones have been investigated. The main criteria that determine the effectiveness of using these zones have been established. Zones that are optimal from the viewpoints of the maximum armature winding EMF and the minimum content of its highest harmonic components have been revealed. The possibility of using the inductor generators for direct connection to the grid has been shown. Recommendations as to the practical use of the investigation results have been given.

Further optimization for rotor tooth shape can be done taking into account the established magnetic field line path in the airgap. For further analysis FEA calculations should be used. Coil end connection influence on higher harmonic content has not been taken into account in the study. Three-dimensional finite element analysis can be performed to set dependencies for higher harmonic content to coil end connections.

ACKNOWLEDGEMENTS

The research has been developed within the framework of Doctoral studies grant of Riga Technical University.

REFERENCES

1. Zhezherin, R. (1961). *Inductor generators*. Moscow: GEI (in Russian).
2. Aleksejeva, M. M. (1967). *Machine generators with increased frequencies*. Latvia: Energija.
3. Dombur, L. E. (1984). *Axial inductor generators*. Riga: Zinatne.
4. Steven, A. E. (2010). Salient pole shoe shapes of interior permanent magnet synchronous machines. In *2010 XIX International Conference on Electrical Machines (ICEM)*, Rome, Italy: IEEE.
5. Deaconu, S. I., Tulelea, L., Popa, G. N., Popa, I., & Abrudean, C. (2008). Optimizing the design of a reactive homopolar synchronous machine with stator excitation. *Industrial Electronics, 2008. IECON 2008. 34th Annual Conference of IEEE*, Orlando, FL, USA: IEEE.
6. Kutt, F., Michna, M., Kostro, G., Ronkowski, M., & Adamczyk, D. (2014). Synchronous generator model taking into account the non-uniform saturation of the pole shoes. In *2014 International Conference on Electrical Machines (ICEM)*, Berlin: IEEE.
7. Boldea, I. (2006). *Synchronous generators*. Boca Raton, FL: CRC Press.
8. Pyrhönen, J., Jokinen, T., & Hrabovcova, V. (2008). *Design of rotating electrical machines.* Chichester: John Wiley & Sons, Ltd.
9. Santalov, A. M., & Serebryakov, A.D. (1976). On the optimal geometry of the tooth zone of inductor machines. *In Proceedings of RKIIGA* (Vol. 113, pp. 12–23). Riga (in Russian).
10. Levin, N. N., & Serebrjakov, A. D. (1976). *Electrical machines and devices*. Riga.
11. Serebrjakov, A. D. (1982). *Optimal tooth zone of inductor motor – Brushless electrical machines*. Riga: Zinatne.
12. Levin, N. N., & Serebrjakov, A. D. (1974).*Tooth zone parameter influence on speed of response for motionless electrical motor*. Riga.
13. Buls, B.K. (1964). *The basics of theory and calculations for magnetic field*. Moscow: Energija.
14. Bronstein, I. N. (1957). *Handbook of mathematics*. Moscow: Gostekhizdat.
15. Flux2D software, (2016). [Online]. Available at http://www.cedrat.com.
16. Gulbis, K., & Kamolins, E. (2017). Investigation of synchronous inductor generator with electrically integrated armature and excitation windings for AC and DC power supply. In *58th International Scientific Conference on Power and Electrical Engineering of Riga Technical University (RTUCON)*, Riga, Latvia: IEEE.
17. EN 50160:2010, (2010). *Voltage characteristics of electricity supplied by public electricity networks*.

INDUKTORMAŠĪNAS ZOBU ZONAS EFEKTIVITĀTE

A. Serebrjakovs, E. Kamoliņš, K. Gulbis, K. Sējējs

K o p s a v i l k u m s

Autori apskata vairākus desmitus induktormašīnu rotora zobu un rievu formas, lai tiktu sasniegta maksimālā enkura tinuma EDS vērtība ar minimālu augstāko harmoniku saturu, kā rezultātā iespējams palielināt mašīnas īpatnējo jaudu un lietderības koeficientu.

Pētījuma ietvaros aprēķini tiek veikti ar analītisku metodi un galīgo elementu metodi, kur galīgo elementu metode ņem vērā gan elektrotehniskā tērauda magnētisko piesātinājumu, gan magnētiskā lauka līniju sadalījumu. Abu aprēķinu galvenie dati ir apkopoti pētījuma rezultātos. No iegūtajiem rezultātiem var secināt, ka vairumā gadījumu analītiskā metode nav pielietojama kvalitatīvai EDS augstāko harmoniku sastāva noteikšanai, jo magnētiskā lauka līnijas plaknē nenoslēdzas paralēli un to sadalījums ir tieši saistīts ar zobu zonas konfigurāciju.

Pētījuma rezultāti parāda, ka induktorģeneratorus ir iespējams izmantot tiešai pieslēgšanai pie energoapgādes tīkla.

18.05.2018.

sciendo

LATVIAN JOURNAL OF PHYSICS
AND TECHNICAL SCIENCES
2018, N 3

DOI: 10.2478/lpts-2018-0017

SOFTWARE ALGORITHM SYNTHESIS FOR DIESEL ELECTRONIC CONTROL UNIT

A.Prohorenko[1], P. Dumenko[2]

[1]National Technical University "Kharkiv Polytechnic Institute"
2 Kyrpychova Str., Kharkiv, 61002, UKRAINE
[2]DiGas Ltd.
31 Talsu soseja, K-17-34, Jurmala, LV-2016, LATVIA
e-mail: p.dumenko@digasgroup.lv

Nowadays global engine construction gets significant progress at a technological level, but specified manufacturers do not release any information about the composition, the structure of the algorithms and the software used by their equipment. It is possible to obtain information only fragmentary and, for example, the description of the electronic control unit algorithm is completely missing. This is a barrier for small companies to improve and adjust existing engines for specific purposes. The present paper describes and develops algorithm synthesis for an electronic diesel engine regulator. Mathematical modelling of the automatic control system has been carried out within the framework of the research. The results of the research have demonstrated the efficiency and sustainability of automatic electronic control system using the proposed algorithm.

Keywords: *diesel, electronic regulator, mathematical modelling, revolutions, transitional process*

1. INTRODUCTION

As it is known, diesel engine power management is based on forced change in quality of the mixture supplied to a cylinder (the so-called "quality power management") [1]. In practice, the implementation of internal mixture formation leads to the need to control the amount of fuel injected into the cylinder, which is called cyclic injection. The dosing of this cycle feed is provided by high pressure fuel equipment (FE), which is an essential part of any diesel engine. Thus, the task of managing a diesel engine is basically up to its fuel equipment management.

Conventional mechanical management system of crankshaft speed with a variety of devices ensures a sufficiently high precision cycling dosage of fuel supply at different diesel engine speeds. However, it has limited features and ignores many external factors that affect its functioning. In addition, the minimum response time of mechanical system is limited to its design [2], [3].

Significant progress in global engine building was achieved through the use of electronic components to manage the components and systems in modern engine designs. Electronic control of diesel engine fuel supply allows the injection process parameters to be controlled accurately and differentially. This is the only way to comply with numerous requirements that are put before modern diesel engines [4].

However, mass production and equipment of diesel engines with electronically controlled fuel equipment is the prerogative of several leading world manufacturers, primarily Bosch, Heinzmann (Germany), Delphi (USA), Motorpal (Czech Republic) and several others. Monopoly ownership of these technologies allows these manufacturers to make super-profits, overstating reasonable costs of such systems as well as the works on their adaptation to the management object. Therefore, it is natural that the specified manufacturers do not release any information about the composition, the structure of the algorithms and the software used by their equipment. The same approach to business is kept by small private companies engaged in fitting electronic management to conventional fuel equipment.

Available open sources and publications only disclose that electronic diesel engine management system includes a set of sensors in a particular configuration. Usually these are the following: engine speed sensor, position sensor (both are obligatory), sensor of the position of high pressure fuel pump rail; temperature fuel, boost pressure, boost temperature, exhaust gases and coolant temperature sensors; executive mechanism in the form of an electromagnet, linear piezoactuator or step motor; electronic control unit (ECU) that connects sensors and executive components by means of its algorithm [4]. However, the description of the ECU algorithm is completely missing. Fragmentary it is known that it processes signals from the sensors and based on the interpolation of the tables in its memory sends control signals to the actuators [4]. Typically, the sets of tables, their purpose and method of forming control signals are not disclosed as commercial secrets (know-how) of the manufacturers.

Therefore, it is relevant to solve scientific and technological problems to create an open source algorithm for a diesel engine power management system for fuel supply, which is the goal of the present article.

2. THE AREA AND METHOD OF RESEARCH

Modern diesel engine fuel systems are divided into two types: fuel equipment with mechanic slide dosage valve drive (cutoff edge on plunger) and FE with solenoid-valve, independent of the plunger movement dosage values of cycle fuel supply. It is clear that the first type can be controlled both mechanically and electronically, while the second one can only be electronic [5]. Advantages and disadvantages of the first and second types of FE are well described in the literature (e.g. [4]), and, therefore, there is no point to focus on it thoroughly in the present paper.

It should be kept in mind that in order to create an electronic system to manage an internal combustion engine, it is necessary to solve tasks from different fields of knowledge. First of all, the system creation requires knowledge of electronics and mechatronics for the development and production of principal and assem-

bly schemes, component selection, as well as selection of the set of sensors and actuators. In addition, the algorithm synthesis and programming code of the ECU processor require the knowledge of the theory of internal combustion engines, the theory of automatic control and low-level programming. Thus, it is possible to admit that the task of development of electronic diesel engine management system is only possible using a synergistic approach in the first place.

3. SETTING UP RESEARCH PROBLEMS

Description of theoretical foundations of electronic diesel engine management and the need for individual sensors are considered in the studies [7], [8]. At first glance, it seems that based on the theory of ICE and the theory of automatic control it does not take a lot of effort to synthesise the necessary algorithm. However, real-life implementation encounters necessary unambiguous matters. For example, the implementation of the proportional integral-differential (PID) regulation (and the theory of automatic control tells us that the majority of electronic controls are based on such an algorithm [6]), is based on the known residual value, i.e., the deviation of the current controlled variable value from the required or desired one. In the case of a diesel regulator, this is the deviation of the current speed of the crankshaft from the desired one. But in order to define the "desired" speed of the engine, working by speed or regulatory (static) characteristics it is necessary to know or determine the current value of load resistance loaders, which is not only difficult to be measured, but also depends on the regulated parameter value (generally it is considered that the moment of load resistance is proportional to the square of the engine speed [1]). Thus, the problem becomes algorithmically insoluble.

4. MANAGEMENT ALGORITHM GROUNDED ON BASE TABLES AND PID CONTROLLER

A rather simple and obvious solution to the problem mentioned above is the use of the calculation of the load resistance moment with the help of the dynamic mathematical model of the engine to be controlled. This model can be introduced into the ECU algorithm and based on the equations of the object movement and statistical table data for its work parameters. Then, the result of the calculation of this mathematical model as the current value of the load resistance moment (M_c) is transmitted into a tabular interpolation algorithm to determine the engine speed n_p, which corresponds exactly to the stable operational mode for the obtained value M_c. This value n_p will be necessary (specified), i.e., "desired" for the engine. Next, comparing the obtained value n_p to the readings of the current engine speed sensor n_i, the residual value is received for the PID controller algorithm, which calculates the signal to the fuel supply actuator.

Accordingly, an appropriate algorithm of the ECU should be based on a set of base tables and special formulas, including PID controller formula and the internal mathematical model predictive equation:

- $V_c = f\left(Hp, n_i\right)$ – basic fuel supply table, dependence of volumetric cyclic

fuel supply by HPFP (V_c) on rail position (Hp) and engine speed;

- $B_c = f\left(V_c, T_{Ton}\right)$ – table (formula) of fuel density, dependence of mass cyclic fuel supply by HPFP (B_c) on volumetric cyclic feed and its temperature (T_{Fuel});
- $M = f\left(n_i, B_c\right)$ – basic engine torque table, the dependence of engine torque (M) on engine speed and mass cyclic fuel supply;
- $M_c = f\left(M, n_i, n_{i-1}\right)$ – the equation of internal mathematical model, which connects the current engine torque (M) and the change of crankshaft speed (n_i , n_{i-1}) the moment of load resistance (M_c) (n_{i-1} – previous (at the previous calculation cycle) value of the crankshaft speed sensor);
- $n_p = f\left(X, M_c\right)$ – table of equilibrium rotational frequencies;
- $Hp_i = Hp_{i-1} - Kp\left(n_i - n_p\right) - Kd\left(n_i - n_{i-1}\right) - Ki\sum_{k=1}^{Ni}\left(n_i - n_p\right)_k$ – current relative position of the HPFP rail by PID control (Kp, Kd, Ki, Ni – specified values of PID-controller).

Then the table interpolations and calculations in the ECU algorithm are to be carried out cyclically in such a sequence.

The beginning of the cycle. According to the values of the engine speed sensor and HPFP rail position (parameters that uniquely determine the mode of engine operation) from the table $V_c = f\left(Hp, n_i\right)$ using two-dimensional linear interpolation the volumetric cyclic fuel supply required for this mode is calculated. This table can be experimentally obtained from the hydraulic characteristics of high pressure fuel system [7]. An example of such a table can be found in Fig. 1.

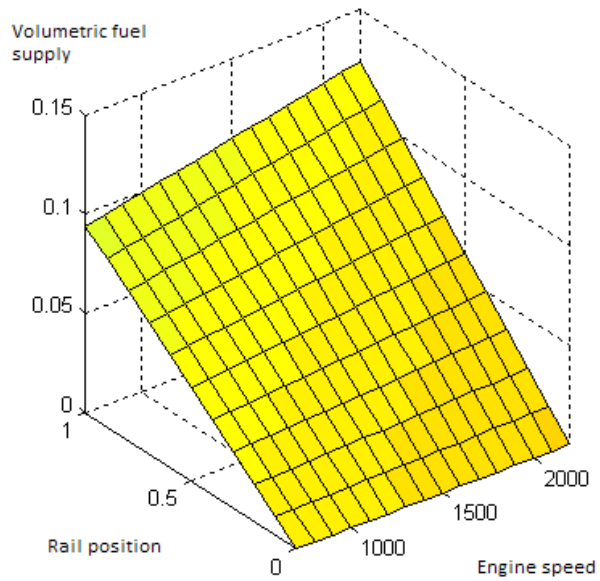

Fig. 1. An example of a basic fuel supply table.

By the found value of the volumetric cyclic fuel supply (V_c) and the data of the fuel temperature sensor (T_{Fuel}) from the table $B_c = f\left(V_c, T_{Fuel}\right)$ corresponding mass cyclic fuel supply is determined. An example of such a table is shown in Fig. 2. In fact, this table is a fuel density table and can be replaced with the formula that relates the fuel density to its temperature, for example, $B_c = V_c\left(\rho_{20} - 0{,}000725 \cdot \left(T_{Fuel} - 20^{\circ}\right)\right)$, where ρ_{20} – the fuel density under normal conditions.

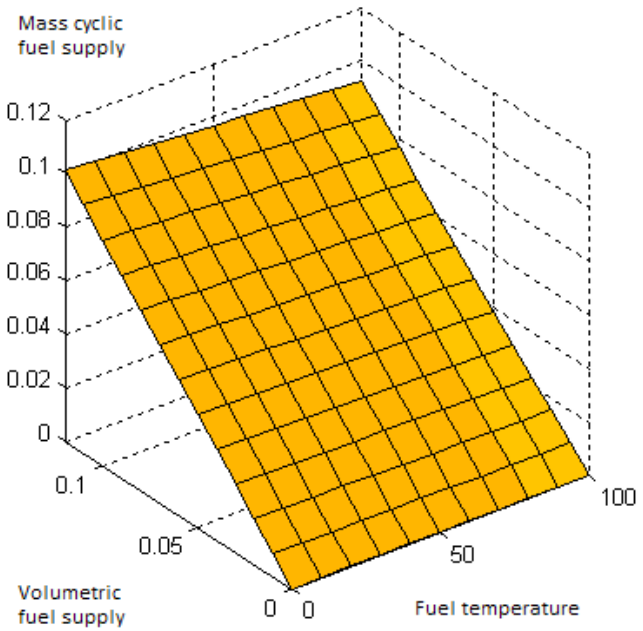

Fig. 2. Correction table by fuel temperature.

By the found value of the mass cyclic fuel supply (B_c) and the current data from the engine speed sensor (n) from the table $M = f\left(n_i, B_c\right)$ current efficient engine torque is determined. Basic engine table $M = f\left(n_i, B_c\right)$ is determined experimentally, for example, according to the measured load characteristics [7]. Such a table is possible to see in Fig. 3. Table contains static engine characteristics.

Basic equation of internal predictive mathematical engine model enables us to determine the current value of loading resistance moment by the relation $M_c = f\left(M, n_i, n_{i-1}\right)$. It is shown below how to derive this relation, hereon the basic equation of internal predictive mathematical model.

Using the data from the control sensor (pedal or lever) (X) and the calculated value of the current loading resistance moment (M_c) by the table $n_p = f\left(X, M_c\right)$ balanced engine speed is determined as the desired parameter. An example of such a table is shown in Fig. 4. It should be noted that the creation of this table is very difficult. It can be obtained having re-orientated the table of balanced engine modes $M = f\left(X, n\right)$ that in its turn is to be determined experimentally.

PID-controller algorithm calculates the necessary position of the HPFP rail *Hp* and then the ECU sends a proportional control signal to the rail actuator mechanism.

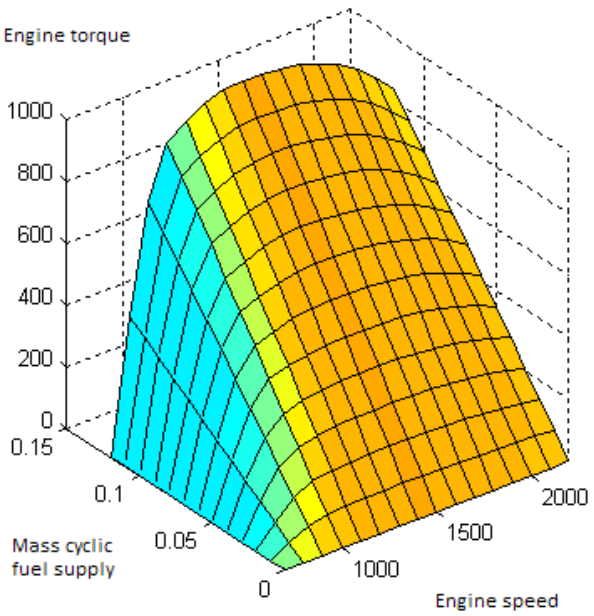

Fig. 3. An example of a basic engine table.

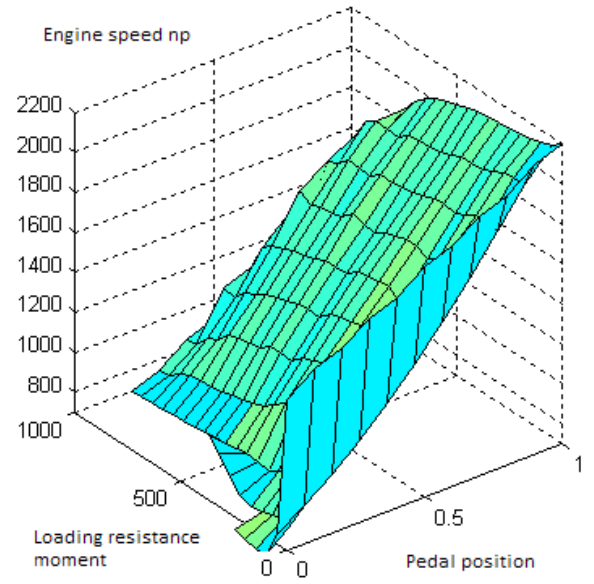

Fig. 4. An example of a balanced engine speed table.

End of cycle. The algorithm described above has a significant advantage, which is a possibility to use PID control in order to achieve necessary quality of transitional processes depending on engine purpose, mode of operation, technical condition and environmental conditions. Thus, it will allow such a management system to be created, which is close to adaptive.

However, this algorithm has also drawbacks. Among them there is a necessity of massive experimental research for filling in basic tables, as well as identifica-

tion of internal mathematical model and PID controller adjustments. Moreover, in practice, there will be deviations of an individual engine options from others, which requires experimental modifications of base tables to fit a particular design. It should also be kept in mind that the parameters of the engine in the table (in particular – the effective engine torque) depend on the thermal state of the engine, environmental conditions, fuel quality, technical condition of the components, etc. For consideration of these conditions the algorithm may require the introduction of additional tables, adjusting coefficients etc. that will inevitably lead to its complication.

5. BASIC EQUATION OF THE INTERNAL MATHEMATICAL MODEL

The equation to predict the engine loading resistance moment value can be deduced in the following way.

The known equation of engine dynamics, which in fact is the second Newton's law for rotational movement, taking into account D'Alamber's principle [3]:

$$J\frac{d\omega}{dt} = M - M_c\,, \tag{1}$$

where J – the inertia mass moment of the rotating engine parts, ω – the current angle crankshaft speed, M – the engine torque, M_c – the loading resistance moment.

It is obvious that $\omega = d\varphi/dt$, where φ – the current angle of the crankshaft turn. Then the equation (1) can be put down in the following manner:

$$J\omega\frac{d\omega}{d\varphi} = M - M_c\,. \tag{2}$$

Getting from minor to final increments of variables, it is possible to indicate $\omega \approx \omega_{cp} = \left(\omega_i + \omega_{i-1}\right)/2$, which is the average angular velocity for two previous measurements ω_i and ω_{i-1}. Taking into account that the increase of the angular velocity for two previous measurements is $\Delta\omega = \omega_i - \omega_{i-1}$ and inserting everything into expression (2):

$$J\frac{\omega_i + \omega_{i-1}}{2}\cdot\frac{\omega_i - \omega_{i-1}}{\Delta\varphi} = M - M_c\,. \tag{3}$$

It is possible to see that the numerator on the left is the difference of squares:

$$J\frac{\omega_i^2 - \omega_{i-1}^2}{2\cdot\Delta\varphi} = M - M_c\,. \tag{4}$$

The known correlation of the angular velocity to the engine speed is $\omega = \frac{\pi}{30}n$. Using it in equation (4) it is possible to obtain:

$$\frac{J}{2\cdot\Delta\varphi}\left(\frac{\pi}{30}\right)^2\left(n^2 - n_0^2\right) = M - M_c\,. \tag{5}$$

Getting to the degree of the crankshaft turn increment $\Delta\varphi = \Delta\varphi^\circ \cdot \frac{\pi}{180}$, and inserting it into (5):

$$\frac{\pi^2 J\left(n^2 - n_0^2\right)}{1800 \cdot \Delta\varphi^\circ \cdot \frac{\pi}{180}} = M - M_c . \tag{6}$$

After shortenings it is possible to obtain the following expression:

$$\frac{\pi J}{10 \cdot \Delta\varphi^\circ}\left(n^2 - n_0^2\right) = M - M_c . \tag{7}$$

Thus, it is possible to determine the desired value of the loading resistance moment:

$$M_c = M - \frac{0{,}314 \cdot J}{\Delta\varphi^\circ}\left(n^2 - n_0^2\right). \tag{8}$$

And this is the expression to be used for calculations in engine management algorithm, where $\Delta\varphi^\circ$ is constant, which can be equal to $\Delta\varphi^\circ = 360^\circ$ or 720°.

6. SIMULATION RESULTS OF TRANSITIONAL PROCESSES

For preliminary confirmation of the accuracy of the suggestions mentioned above, the authors of the present paper carried out calculation studies of diesel engine transitional processes provided by the proposed electronic regulator algorithm. The calculations were carried out according to the mathematical model of diesel engine management system described in the paper [5]. A virtual diesel engine was selected as an example for calculation purposes. It was accepted that the initial balanced operation mode had the following parameters: control position $X_0 = 0.7$, engine speed $n_0 = 1640$ rpm. The authors also studied the reaction of the engine management system to external independent controlling and activating influence.

System reaction to controlling influence. At the moment of time t = 1 sec, a controlling influence is applied to the system by moving the control by a relative number $\Delta X = 0.2$. At the same time, a speed transitional process shown in Fig. 5 takes place. It is possible to see the values of the current balanced engine speed (dashed line), which are calculated using the internal mathematical algorithm model. As it can be seen in Fig. 5, as a result of the transitional process in 2 seconds the engine accelerates to $n = 1930$ rpm and reaches a new balanced mode, which is evidence of correct functioning of the proposed regulator algorithm.

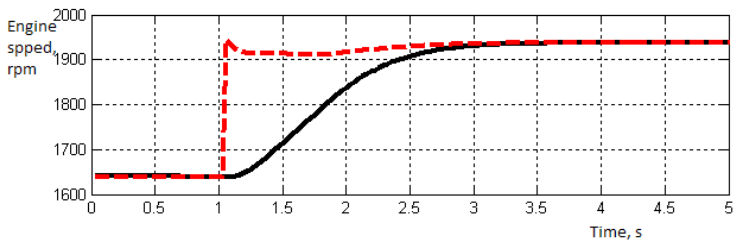

Fig. 5. Speed transitional process under control.

The movement of the HPFP rail during this transitional process is shown in Fig. 6. As it can be seen, in the transitional process the engine (HPFP rail) does not reach external speed characteristics like it often takes place while working with a mechanical all-mode regulator.

System reaction to activating influence. At the moment of time t = 1 sec, an activating influence is applied to the system in the form of loading resistance moment increase by the value $\Delta M_c = 200$ N×m. At the same time, a speed transitional process shown in Fig. 7 takes place. It is possible to see the values of the current balanced engine speed (dashed line), which are calculated using the internal mathematical algorithm model. As a result of the transitional process, in 2 seconds the engine reaches a new balanced mode $n = 1577$ rpm, which is evidence of correct functioning of the proposed regulator algorithm.

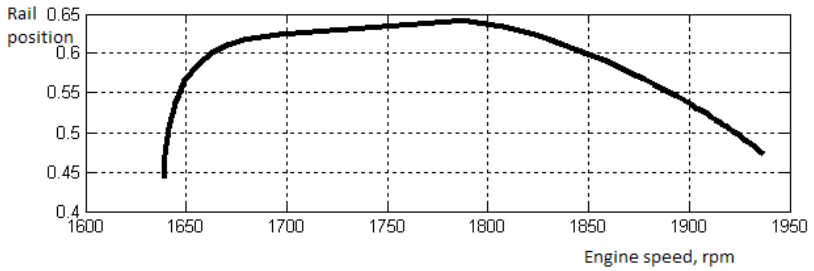

Fig. 6. HPFP rail movement in the transitional process under control influence in the frequency area.

The HPFP rail movement in the transitional process in the frequency area is shown in Fig. 8. The HPFP rail movement in transitional process takes place along certain control characteristics.

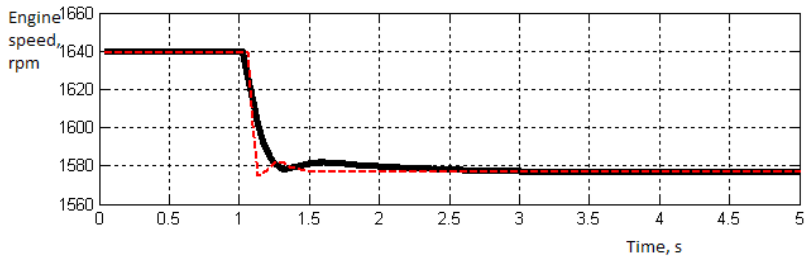

Fig. 7. Speed transitional process under activating influence.

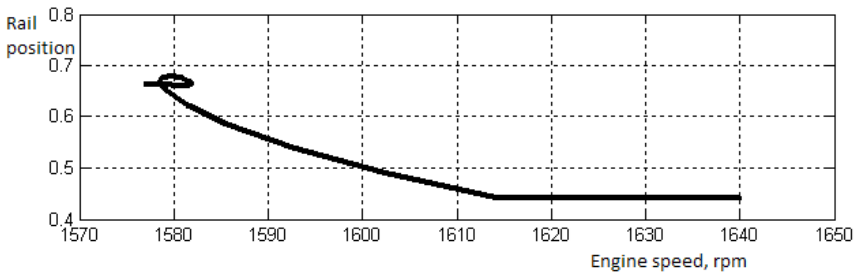

Fig. 8. HPFP rail movement in the transitional process under activating influence in the frequency area.

The presented algorithm of electronic diesel engine management systems has prospects in the following areas:

- *Creation of control algorithms for turbocharged engines.* Implementation of the dependence of fuel supply on boost pressure is only a limiting factor aimed at smoke reduction and engine torque reduction during acceleration. In the first approach, this dependence can be described in additional tables of current cyclical supply limitation by airflow such as $B_c = f\left(G_{Air}, n\right)$.
  The management of injection advance angle, gas recycling, turbocharger and several other matters can also be successfully solved while developing this algorithm.
- *Management algorithm adaptation in diesel engines with electronic valve actuator of the fuel equipment.* This algorithm can manage diesel engines with electromagnetic injectors or HPFP and even Common-Rail system. In this case, the signal sent by the controller in form of the position of the fuel rail is substituted by the time signal sent to the corresponding actuator. However, the Common-Rail system requires taking into account the dependence of the cyclic supply amount on the fuel pressure in the accumulator, which can be solved using additional basic tables such as $V_c = f\left(\tau_{inj}, p_{Fuel}\right)$ and $p_{Ton} = f\left(X, n\right)$.

7. CONCLUSIONS

1. The research has developed and described the concept of open algorithm synthesis for electronic diesel engine control based on basic tables and PID-control.
2. The research has deduced the basic equation of internal predictive mathematical model of the algorithm, which connects current engine torque and engine speed change to loading resistance moment.
3. Calculation studies by mathematical model have demonstrated workability and stability of the system engine-load under this algorithm.

ACKNOWLEDGEMENTS

The research leading to these results has been supported by the European Regional Development Fund project "Development of Competence Centre of Mechanical Engineering", contract No.1.2.1.1/16/A/003 signed between Competence Centre of Mechanical Engineering and Central Finance and Contracting Agency, Research No. 3.2 "Dual Fuel System Development for a Diesel Engine Locomotive".

REFERENCES

1. Vyrubov, D. N., Ivashchenko, N. A. & Ivin, V. I. (1983). *Internal combustion engines. Theory of piston and combined engines: Workbook for higher technical educational establishments*. M.: Machine-building.

2. Prokhorenko, A. A. (2014). *Automatic management of internal combustion engines (tuition manual)*. Kharkiv: Pidruchnyk NTU KhPI.
3. Krutov, V.I. (1989) *Automatic management and control of internal combustion engines*. M.: Machine-building.
4. *Diesel engine management systems.* (2004). M.: JSC "Magazine "Za rulyom".
5. Prokhorenko, A. A. (2015). Mathematical description of diesel engine AMS with electronic regulator in the environment of conditions. *Internal Combustion Engines*, *1*, 14–20.
6. Besekerskiy, V. A., & Popov, E. P. (2003). *Theory of automatic management systems*. Saint-Petersburg: Publishing House "Profession".
7. Prokhorenko, A. O., & Meshkov, D. V. (2008). Basic fuel management characteristics of Common Rail diesel engines. *Internal Combustion Engines*, *2*, 39–43.
8. Prokhorenko, A. O. (2009). Algorithm of Common Rail diesel engines fuel management. Theoretical elements. *Internal Combustion Engines*, 2, 69–74.

DĪZEĻMOTORA VADĪBAS BLOKA PROGRAMMATŪRAS ALGORITMA SINTĒZE

A. Prohorenko, P. Dumenko

K o p s a v i l k u m s

Mūsdienās globāla iekšdedzes motoru ražošana saskaras ar nozīmīgu progresu tehnoloģiskā līmenī, bet noteikti ražotāji neizplata informāciju par algoritmu struktūru, sastāvu un izmantoto programmatūru. Ir pieejama tikai fragmentāra informācija, un, piemēram, elektroniskā vadības bloka algoritma apraksts pilnībā nav pieejams. Tas traucē mazajām kompānijām veikt esošo motoru uzlabošanu un pielāgošanu konkrētiem mērķiem.

Raksta autori raksturo dīzeļmotora elektroniskā regulatora algoritma sintēzi. Pētījuma laikā ir veikta automātiskās kontroles sistēmas modelēšana. Iegūtie rezultāti parāda automātiskās elektroniskās kontroles sistēmas efektivitāti un ilgtspējību, ieviešot konkrēto algoritmu.

25.03.2018.

sciendo

LATVIAN JOURNAL OF PHYSICS
AND TECHNICAL SCIENCES
2018, N 3

DOI: 10.2478/lpts-2018-0018

SIMULATION OF SEISMIC EXPLOSION WAVES WITH UNDERGROUND PIPE INTERACTION

N.Remez[1], A.Dychko[1], S.Kraychuk[2], N.Ostapchuk[2], L.Yevtieieva[1], V.Bronitskiy[1]

[1]Institute of Energy Saving and Energy Management, National Technical University of Ukraine "Igor Sikorsky Kyiv Polytechnic Institute"
37 Peremohy Ave., Kyiv, 03056, UKRAINE
[2] Department of Economic Cybernetics, Rivne State University of Humanities
12 Stepana Bandery Str., Rivne, 33000, UKRAINE

The present paper provides numerical simulation of interaction of wave processes in the system "soil massif – underground pipeline" in explosion of charge on the surface of ground. Construction is considered in the framework of nonlinear theory of shells of Tymoshenko type. Soil is modelled by a solid porous multicomponent visco-plastic medium. The study establishes patterns of changes in stress-strain state of system depending on depth of pipeline laying and its diameter.

Keywords*: distraction, explosion, numerical simulation, underground pipe*

1. INTRODUCTION

Supply of oil, gas, drinking water, drainage is one of the necessary conditions for urbanised areas. Usually these benefits of civilization are transmitted and distributed through pipelines. At the same time, different variations of pipes are used in construction and for transfer of water, gas and oil through distributive systems. All these pipes are earthed in soil to protect them from adverse environmental factors and dynamic effects of various nature: earthquakes, explosions, vibrations from transport and working machines, diversions. But such loads on a pipeline as effect of weight of soil mass, fluid pressure, etc. are increased with earth.

Different factors, such as soil properties, intensity of soil fluctuations, internal pressure of pipe, its dimensions, including diameter and thickness of wall, parameters and nature of dynamic loads have a consistent effect on stability of underground pipelines [1]–[2]. Therefore, when calculating the stress-strain state, fluctuations of the pipeline-soil system should be considered. Its dynamic characteristics are different from the dynamic characteristics of the pipeline separated conditionally from soil environment.

Most studies of the dynamic effect on underground pipelines are devoted to impact of earthquakes and seismic waves of various nature [3]–[6].

2. NUMERICAL SIMULATION

The goal of the research is to determine the effect of explosive action of surface charge on underground pipeline. When modelling it is assumed that charge of explosives detonates on surface of soil. At the same time, an explosive wave propagates into soil massif with pipeline, located inside.

In the cylindrical coordinate system *r, z* equations of motion of soil within the framework of mechanics of continuous medium have the form:

$$\frac{\partial \sigma_{rr}}{\partial z} + \frac{\partial \tau_{rz}}{\partial r} + \frac{\tau_{rz}}{r} = \rho \frac{du}{dt}, \tag{1}$$

$$\frac{\partial \tau_{rz}}{\partial z} + \frac{\partial \sigma_{zz}}{\partial r} + \frac{\sigma_{zz} - \sigma_{\theta\theta}}{r} = \rho \frac{dw}{dt}, \tag{2}$$

$$\frac{1}{V}\frac{dV}{dt} = \frac{\partial u}{\partial z} + \frac{\partial w}{\partial r} + \frac{w}{r}, \qquad V = \frac{\rho_0}{\rho}, \tag{3}$$

$$u = \frac{dz}{dt}, \; w = \frac{dr}{dt}, \tag{4}$$

$$\sigma_{zz} = S_{zz} - P, \; \sigma_{rr} = S_{rr} - P, \quad \sigma_{rr} = S_{rr} - P, \tag{5}$$

$$P = \frac{1}{3}\left(\sigma_{rr} + \sigma_{\theta\theta} + \sigma_{zz}\right), \tag{6}$$

where $\sigma_{rr}, \sigma_{\theta\theta}, \sigma_{zz}, S_{rr}, S_{\theta\theta}, S_{zz}$ – components of tensor and deviator of stress tensors; τ_{rz} – tangential stress, τ_{rz} – initial and current density of medium, t – time.

The soil is modelled by a solid porous multicomponent visco-plastic medium with a constant viscosity coefficient [7], and its equation of dynamic volume compression and discharge has the following form:

$$\dot{\varepsilon} = \varphi(P,\varepsilon)\dot{P} - \frac{\alpha_1 \lambda(P,\varepsilon)}{\eta}\psi(P,\varepsilon). \tag{7}$$

Functions included in equation (7) for loading and unloading S_i are different and determined according to [7].

The condition of soil plasticity is the modified condition of Mises–Botkin [8].

The theory of shells of the Tymoshenko type and physical relations of differential plasticity theory with linear kinematic hardening are used to describe dynamic behaviour of the pipeline [9], [10]. Equations of fluctuations for a cylindrical shell have the form:

$$\frac{\partial T_{11}}{\partial x} = \rho\ h\ \frac{\partial^2 u_1}{\partial t^2},$$

$$\frac{\partial \overline{T}_{13}}{\partial x} - \frac{T_{22}}{R} + P_3\ (x,t) = \rho\ h\ \frac{\partial^2 u_3}{\partial t^2}, \tag{8}$$

$$\frac{\partial M_{11}}{\partial x} - T_{13} + P_3\ (x,t) = \rho\ \frac{h^3}{12}\frac{\partial^2 \phi_1}{\partial t^2}\ .$$

Expressions for the values of forces-moments are the following:

$$T_{11} = B_{11}(\varepsilon_{11} + \nu_{21}\varepsilon_{22}),$$

$$T_{22} = B_{22}(\varepsilon_{22} + \nu_{12}\varepsilon_{11}), \tag{9}$$

$$T_{13} = B_{13}\varepsilon_{13}, \qquad M_{11} = D_{11}\kappa_{11}\ ,$$

where

$$\varepsilon_{11} = \frac{\partial u_1}{\partial x} + \frac{1}{2}[\theta_1]^2,\ \varepsilon_{22} = \frac{u_3}{R},\ \ \varepsilon_{13} = \varphi_1 + \theta_1,\ \theta_1 = \frac{\partial u_3}{\partial x},\ \kappa_{11} = \frac{\partial \varphi_1}{\partial x}\ ; \tag{10}$$

$$B_{11} = \frac{E_1 h}{1-\nu_{12}\nu_{21}},\ \ B_{22} = \frac{E_2 h}{1-\nu_{12}\nu_{21}},\ B_{13} = G_{13}h\ ,\ D_{11} = \frac{E_1 h^3}{12(1-\nu_{12}\nu_{21})}\ . \tag{11}$$

In formulas (8)–(11), the following designations are taken: ρ, h, R – density of material, thickness and radius of pipe; u_1, u_3, ϕ_1 – components of generalised vector of displacements; T_{11}, T_{13}, T_{22}, M_{11} – components of tensors of forces and moments; P_3 – pressure; ε_{11}, ε_{22}, ε_{13} – components of deformation tensor; E_1, E_2, ν_{12}, ν_{21}, G_{13} – elastic constants of pipeline material.

In the case of plastic deformations, relationships between corresponding deformations and stresses are written in the form of incremental theory of plasticity with the Mises condition.

Equations (1)–(11) are supplemented by the corresponding initial and limit conditions.

3. RESULTS AND DISCUSSION

With the help of the finite elements method, modelling of soil environment, in which an underground gas pipeline is located, is carried out. For numerical simulation, a calculating grid of 9635 elements is constructed.

It is assumed that the pipeline, which is located in clay soil at a depth of 2.0–6.0 m, is made of steel with the following physical and mechanical characteristics:

yield limit G = 240 N / m^2, Poisson coefficient v = 0.3, elasticity modulus E = 240 N / m^2, density = 7855 kg / m^3.

The explosion of charge of 10 kilograms of trotyl on a soil surface is considered. It corresponds to the minimum power of loaded charge, a bomb or a small rocket. Dependence of stress on time on the surface of the soil massif is shown in Fig. 1.

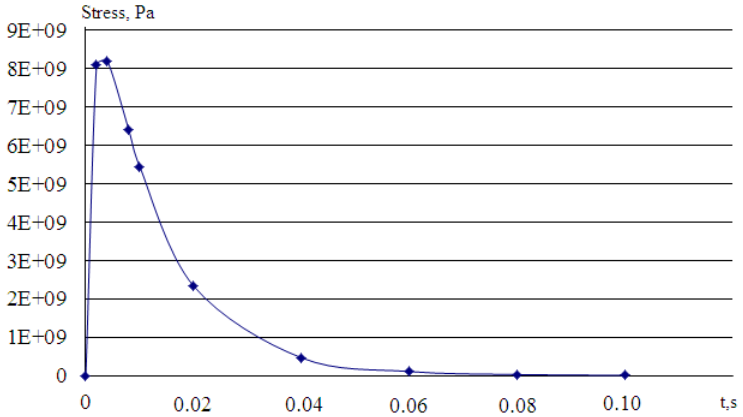

Fig. 1. Dependence of stress on time on the surface of the soil massif.

Isobars of average hydrostatic pressure (in GPa) in plane at different moments of time t = 1.0 s are presented in Fig. 2.

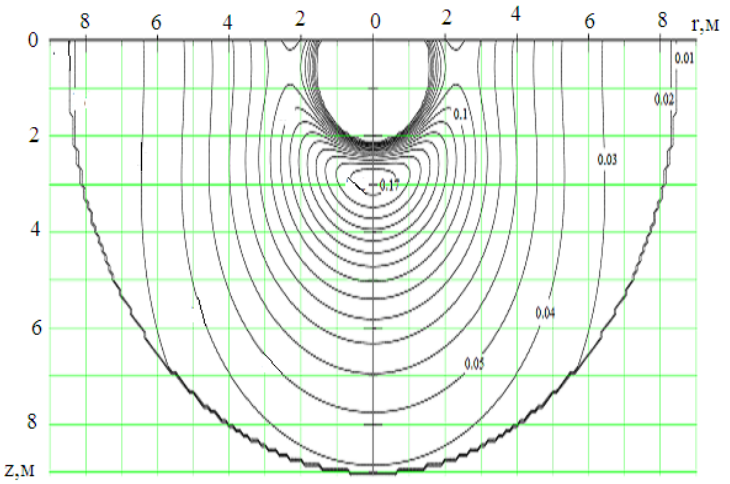

Fig. 2. Isobars of average hydrostatic pressure (in GPa) in plane *rOz* at different moments of time t = 1.0 s.

It is shown in Fig. 2 that the field of isobars is a difficult depiction due to interaction of waves with different limits and angular points, and also between themselves. At the considered moment of time, the greatest load is achieved in gas cavity and in soil near it.

The stress wave, spreading in soil, reaches the pipeline and causes deformation in these media (Fig. 3).

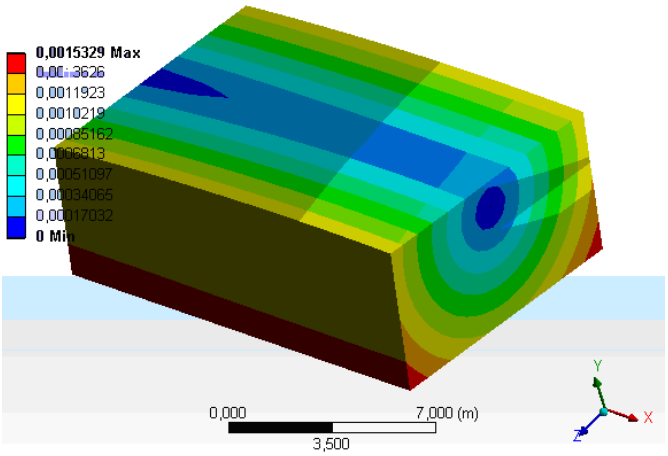

Fig. 3. Distribution of volumetric deformations in soil and pipelines.

Distribution of stresses in a steel pipe of 1.5 m in diameter at a laying depth of 5 m is shown in Fig. 4.

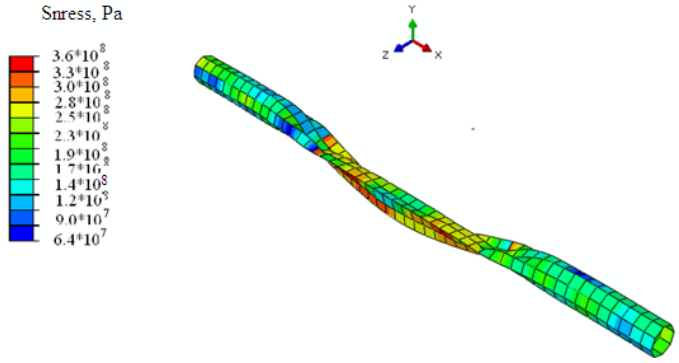

Fig. 4. Distribution of stresses in the steel pipe of 1.5 m in diameter at a laying depth of 5 m.

It is seen from the figure that the maximum stress in the pipeline is reached at 360 MPa, which is significantly greater than the steel yield limit (240 MPa), especially in frontal surface of pipe; therefore, pipeline loses its bearing capacity and is destroyed.

Dependence of stress on pipeline from depth of its laying at different diameters of pipeline: 1 – D=0.4 m, 2 – D=1.5 m is shown in Fig. 5. It is established that with a decrease in diameter, the stress increases, and the pipe undergoes plastic deformation and loses its ability to work.

With an increase in depth of pipeline arrangement, there is a decrease in stresses, but the area of elastic deformations for a pipe with a diameter of 1.5 m starts at a depth of 6 m, and with a diameter of 0.4 m – from a depth of 7 m.

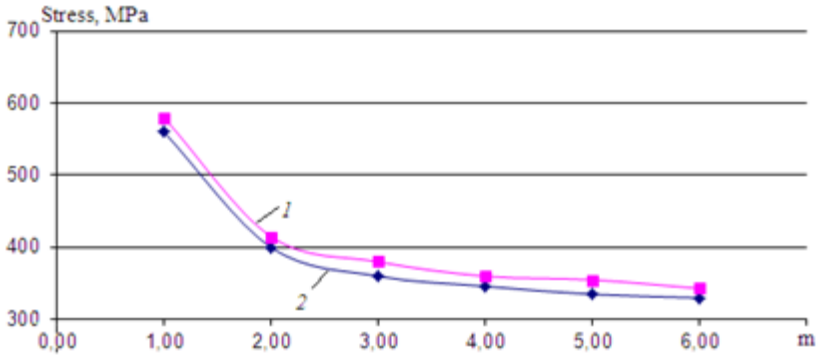

Fig. 5. Dependence of stress on pipeline from depth of its laying at different diameters of pipeline: 1 – D=0.4 m, 2 – D=1.5 m.

Dependences of polynomial stresses on depth of laying the pipeline, which allow carrying out predictive calculations of durability of pipe under different dynamic loads, are obtained:

– for a pipe with a diameter of 1.5 m:

$$\sigma = -5.92y^3 + 78.04y^2 - 337.76y + 882.00,\ Pa;\ R^2 = 0.991,$$

– for a pipe with a diameter of 0.4 m:

$$\sigma = 1.94y^4 - 33.47y^3 + 211.66y^2 - 591.51y + 990.83,\ Pa;\ R^2 = 0.9981.$$

4. CONCLUSIONS

The present study has introduced the methodology of numerical solution to the problem of explosion of a charge of trotyl on the surface of a soil massif with a pipeline placed inside. It makes it possible to investigate regularities of variation of wave processes in heterogeneous "soil–pipeline" system.

The authors of the research have developed the mathematical model, algorithm and program for a numerical solution to the problem of dynamic change of stress-strain state by "soil massive–underground pipeline" system in explosion, of physical-mechanical characteristics of soil and pipeline material, as well as geometric dimensions of the last one (pipe diameter and thickness).

It has been established that with a decrease in diameter of pipeline the stress increases, and pipe undergoes plastic deformation and loses its efficiency. With an increase in depth of pipeline location, there is a decrease in stress; thus, the area of elastic deformations of a pipe with a diameter of 1.5 m begins with a depth of 6 m, and for a diameter of 0.4 m – from a depth of 7 m.

Polynomial dependences of stresses on depth of laying the pipeline, which allow carrying out predictive calculations of durability of pipe under different dynamic loading, have been obtained in the present research.

Results of the research can be used for determining the safe depth of laying the pipelines of various purposes when they are subject to dynamic shock loads.

REFERENCES

1. Shemyakin, E.I. (1963). About waves of stresses in durable mountains rocks. *PMTF*. 3, 83–93.
2. Borovikov, V.A., & Vanyagin I.V. (1976). To the calculation of stress wave parameters at explosion-prolonged charge in rocks. *Explosive Affair*, *76*(33), 74–85.
3. Jeremy, I. (1978). Underground pipeline behaviour under seismic loading. In Division, A.G.E. (Ed.), *Earthquake engineering and soil dynamics*. New York, American Society of Civil Engineers.
4. Golbahar Haghighy, M. V., & Agha Kuchak, E. A. (2006). Analysis of marine pipe lines subjected to the loading caused by propagation of seismic wave and fault displacement, *Marine Engineering Magazine*.
5. Leon, R. L., & Wang, M. (1978). Performance of underground pipelines in earthquake, In Division, A. G. E. (Ed.), *Earthquake engineering and soil dynamics*. New York, American Society of Civil Engineers.
6. Remes, N. S., Ivanova, I. A., & Demeschuk, N. S. (2014). Interaction of seismic waves with layered soil array and underground pipelines. *Visnyk NTUU "KPI", series "Mining", 24,* 27–34.
7. Luchko, I. A., Plaksii, V. A., & Remez, N. S. (1964). Cylindrical blast waves in a solid multicomponent viscoplastic medium. *Explosive Affair, 88*(45), 28–36.
8. Grigoryan, S.S. (1964). To solution of the task of underground explosion in soft soils. *Applied Mathematics and Mechanics, 28*(2), 1070–1075.
9. Timoshenko, S. P. (1937). *Theory of elasticity*. Moscow: ONTI.
10. Lugovoy P. Z., Meish, V. F., & Remez, N. S. (2000). Elastoplastic behaviour of ribbed cylindrical shells under nonstationary loading. *Archives of Civil Engineering, XLVI*, 3, 43–49.

SEISMISKO SPRĀDZIENU VIĻŅU SIMULĀCIJA AR PAZEMES CAURUĻU MIJIEDARBĪBU

Remezs N., Dičko A., Krajčuks S., Ostapčuks N., Jevtejeva L., Bronitskijs V.

K o p s a v i l k u m s

Raksts sniedz skaitlisko simulāciju viļņu procesu mijiedarbībai sistēmā "augsnes masīvs – pazemes cauruļvads" lādiņa sprādzienā uz zemes virsmas. Simulācija tiek pētīta Timošenko tipa čaulu nelineārās teorijas ietvaros. Augsni modelē cietā porainā daudzkomponentu viskozes-plastmasas vidē. Pētījumā tika noteikti sistēmas stresa-deformācijas stāvokļa izmaiņu modeļi atkarībā no cauruļvada novietojuma dziļuma un tā diametra.

26.04.2018.

sciendo

LATVIAN JOURNAL OF PHYSICS
AND TECHNICAL SCIENCES
2018, N 3

DOI: 10.2478/lpts-2018-0019

PHYSICS

NONLINEAR THERMODIFFUSION IN GASES AT MODERATE TEMPERATURES

A.J.Janavičius[1], S.Turskienė[2]

[1] Šiauliai University, 88 Vilniaus Str., LT-76285, Šiauliai, LITHUANIA
e-mail: AYanavy@gmail.com
[2]Computer Science Department, Šiauliai University, 141 Vilniaus Str.,
LT-76353, Šiauliai, LITHUANIA
e-mail: turskienes@gmail.com

The paper discusses the properties of the nonlinear thermodiffusion equation corresponding to the diffusion processes, which occur with a finite velocity. In the previous papers, A. J. Janavičius proposed the nonlinear diffusion equation with the diffusion coefficient directly proportional to the concentration of impurities. This equation provides a more exact description of the profiles of impurities in Si crystals. The heat transfer in gases carries a greater average kinetic energy based on nonlinear diffusion of gas molecules from hot regions to the coldest ones with a finite velocity by random Brownian motions. In this case, the heat transfer in gases can be described by using nonlinear thermodiffusion equation with heat transfer and thermodiffusion coefficients directly proportional to temperature T . The obtained approximate analytical solutions are successfully applied in defining temperature profiles and heat transfer coefficients in gases as well as providing opportunities for practical applications. It has been concluded that heat spreading in gases depends on temperature differences and pressure in gases.

Keywords: *approximate analytical solution, nonlinear thermal diffusion equation, temperature profiles*

1. INTRODUCTION

In the previous papers, we have discussed the nonlinear diffusion of impurities in semiconductors [1], [2], nonlinear thermodiffusion in gasses [3] and heat transfer in metals by electrons [4] using mathematical methods of similarity variables [1] for nonlinear equations. The obtained results are important for engineering applications. We assume that the process of heat transmittance in gasses is similar to nonlinear diffusion processes described as Brownian movement of atoms in solids spreading with a finite velocity. Heat transfer can be described using modified theory of the nonlinear

diffusion in solids [1]. In this case, the frequency of the jumps of diffusing molecules [6] depends upon the coordinates, concentration and temperature. The coefficient of thermal conductivity of gases can be expressed in the following way [6]:

$$K = \frac{1}{3}\lambda \bar{v} c_v \rho = D_m c_v \rho = \frac{k\bar{v}}{2\sqrt{2}\pi d^2}, \lambda = \frac{1}{\sqrt{2}\pi d^2 n}, \bar{v} = \sqrt{\frac{8RT}{\pi\mu}}. \quad (1)$$

Here λ – mean values of a free path of diffusing molecules, $\bar{v}$ – mean velocities of molecular movement, c_v – molar heat capacity at constant volume, ρ – density of gas, n – number of molecules per unit volume, k – Boltzmann constant, T – temperature of gases, μ – molar mass, R – gas constant, d – diameter of a gas molecule, D_m – coefficient of thermal diffusion in gases.

We introduced the equation of thermal conductivity of gases [6] with the nonlinear thermodiffusion coefficient proportional to the temperature:

$$D_n(T) = \frac{K(T)}{\rho \cdot c_p} = \frac{K_e T}{\rho \cdot c_p \cdot T_e} = \frac{k\bar{v}}{\sqrt{2}\pi d^2 p T_e} T = \frac{D_e}{T_e} T(x,t) = D_{en} T(x,t) \quad (2)$$

We introduced the constant pressure $p = n(x,t)kT(x,t)$ for slow heat transmission in gases when decreasing temperature $T(x,t)$ is compensated by increasing concentration $n(x,t)$ of gases.

Using the heat flow j for continuity equation [6], we obtained

$$\frac{\partial T}{\partial t} = -div(-D_n(T)grad(T)), j_p = -D_n(T)\frac{\partial T}{\partial x}. \quad (3)$$

Here constant D_e – thermodiffusion coefficient in environment for the specific heat capacity c_p of gases at constant pressure p, K_e – coefficient of thermal conductivity of environment, T_e – temperature of environment, D_{en} – proportionality constant for nonlinear thermodiffusion function $D_n(T)$.

The nonlinear thermodiffusion equation (3) for temperature $T(x,t)$ $0 \le x \le x_0$, $0 \le t \le t_0$ can be rewritten in a more convenient form

$$\frac{\partial T}{\partial t} = D_{en}\left[\frac{\partial}{\partial x}\left(T\frac{\partial T}{\partial x}\right)\right], \quad (4)$$

which mathematically coincides with nonlinear diffusion equation [1]. The numerical calculations provided in [2] give dependence $n(x,t)$ as a straight line in the region $0 \le x \le x_0$, $0 \le t \le t_0$ and temperature $T(x,t)$ dependence must be similar. The jump of a greeter kinetic energy of hotter molecules to the points $x + \lambda$ is possible only if it exists in the points x. This requirement is equivalent to the approval that thermodiffusion must occur with finite velocity. It is very important for definition of thermal conductivity [3] and diffusion coefficients [1], [2].

The nonlinear heat conduction equation [7] can be rewritten by introducing nonlinear equation

$$\frac{\partial E}{\partial t} = \frac{\partial}{\partial x}(k_e(E)\frac{\partial E}{\partial x}) \tag{5}$$

for energy density E.

The complicated approximate analytical solution [7] $E(x,t)$ of the equation (5) cannot be experimentally measured. In our case, temperatures $T(x,t)$ can be measured directly and compared to theoretical calculations.

2. SOLUTION OF THE NONLINEAR HEAT DIFFUSION EQUATION FOR ONE-DIMENSIONAL CASE

The solution of (4) can be obtained by introducing similarity variable [5] ξ and function $f(\xi)$

$$T(\xi) = T_e f(\xi), \quad \xi = \frac{x}{\sqrt{D_{en} T_e \cdot t}} = \frac{x}{\sqrt{D_e t}}, \tag{6}$$
$$0 \le \xi \le \xi_0, \; 0 \le x \le x_0, \; x_0 = \xi_0 \sqrt{D_{en} T_e \cdot t} = \xi_0 \sqrt{D_e t},$$

which depends on thermodiffusion constant D_e at environment temperature T_e. By substituting (6) into (4), we obtain nonlinear differential equation

$$2\frac{\partial}{\partial \xi}\left(f \frac{\partial f}{\partial \xi} \right) + \xi \frac{\partial}{\partial \xi} f = 0. \tag{7}$$

The solution of this nonlinear equation can be expanded by power series, including boundary condition at maximum value $\xi = \xi_0$

$$f(\xi) = \sum_{n=0}^{\infty} a_n (\xi - \xi_0)^n, \; f(z) = \sum_{n=0}^{\infty} a_n z^n, \quad z = \xi - \xi_0, \; -\xi_0 \le z \le 0. \tag{8}$$

Now equation (7) must be transformed for the new variable z

$$2 \cdot \frac{\partial}{\partial z}\left(f \frac{\partial}{\partial z} f \right) + z \cdot \frac{\partial}{\partial z} f + \xi_0 \frac{\partial}{\partial z} f = 0. \tag{9}$$

By requiring that solution $f(z)$ of nonlinear equation (9) can be expressed by power series, we obtain recurrence relations [8] between coefficients a_n, $n = 0,1,2,...$ (10)

3. THE APPROXIMATE ANALYTICAL SOLUTION

In the approximation by polynomials we used expansion restricted by coefficients a_0, a_1, a_2, a_3. From expression (10) at $n = 0,1,2$ we obtain the following system of equations:

$$4a_2a_0 + 2a_1^2 + \xi_0 a_1 = 0 \ , \tag{11}$$

$$12a_3a_0 + 12a_2a_1 + a_1 + 2\xi_0 a_2 = 0 , \tag{12}$$

$$24a_3a_1 + 12a_2^2 + 2a_2 + 3\xi_0 a_3 = 0 , \quad a_0 = 1 , \tag{13}$$

where in (13) $a_4 = 0$. From the boundary condition $T(0) = T_e f(0)$ at heat maximum penetration point we obtain $f(0) = a_0 = 1$.

The solution $f(z)$ (8) must satisfy the second boundary condition $T(-\xi_0) = T_e f(-\xi_0) = T_S$ at heat source $T(\xi = 0) = T_S$. Then we obtain

$$(T(z) - T_e)/T_e = a_1 z + a_2 z^2 + a_3 z^3 , \ z = \xi - \xi_0 . \tag{14}$$

The expression of temperature (6), (8) at heat source T_S is obtained

$$T = T_e f(-\xi_0) = T_S , \ \sum_{m=1}^{n+1} (-1)^m a_m \xi_0^m = \frac{\Delta T}{T_e} , \ \Delta T = T_S - T_e . \tag{15}$$

The approximate solution

$$f_3(z) = a_0 + a_1 z + a_2 z^2 + a_3 z^3 , \ a_0 = 1 , \tag{16}$$

is used including the boundary condition (15)

$$-a_3 {\xi_0}^3 + a_2 {\xi_0}^2 - a_1 \xi_0 = \frac{T_S}{T_e} - 1 , \ \frac{T_S}{T_e} - 1 = \frac{T_S - T_e}{T_e} = \frac{\Delta T}{T_e} . \tag{17}$$

Thermodiffusion coefficients $D_e = K_e/(\rho \cdot c_p)$ and experimental [9] values of heat conductivities K_e in air at normal pressure $p = 1.013 \cdot 10^5 N/m^2$ and moderate temperatures with specific heat $c_p = 0.999 \cdot 10^3 \frac{J}{kg \cdot K}$ for air density $\rho = 1.293 kg/m^3$ are presented in Table 1.

Table 1

Dependence of Heat Conductivity K_e and Thermodiffusion D_e Coefficients at Temperatures t^oC

t^oC	T, K	$K_e, \frac{10^{-2} J}{smK}$	$D_e, 10^{-2} \frac{m^2}{s}$
27	300.15	2.553	2.172
17	290.15	2.485	2.043
7	280.15	2.417	1.919
-3	270.15	2.348	1.798
-23	250.15	2.207	1.565
-53	220.15	1.983	1.237

Using these meanings of D_e and solving (11), (12), (13), (17), we can obtain the heat penetration depths (6) $x_0 = \xi_0 \sqrt{D_e t}$ and profiles (14) for temperature differences $(T(\xi) - T_e)/T_e$. The coefficients a_1, a_2, a_3, ξ_0 defining solution (16) $f(z)$ are presented in Table 2.

Using solutions (16) presented in Table 2, we see that at less values $\Delta T / T_e$ they can by simplified by taking $a_2 {\xi_0}^2 \approx 0$ and $a_3 {\xi_0}^3 \approx 0$. In this case, the parameter $\xi_0 = -\frac{1}{a_1}(T_S - T_e)/T_e$ can be obtained from (17). The constants a_1, a_2 practically are not changing at different $\Delta T / T_e$. The solutions for $t\ ^0C$=-53 ^0C in two last rows of Table 2 practically coincide. This means that approximate solution with $a_3 = 0$ presented in the last row is sufficiently exact for practical calculations. The constant ξ_0, defining a maximum of heat penetration depths x_0 proportional to $\sqrt{D_e t}$ like for nonlinear diffusion [1], can be expressed approximately

$$x_0 = \xi_0 \sqrt{D_e t}\ ,\ \ \xi_0 \approx -\frac{1}{a_1}(T_S - T_e)/T_e \tag{18}$$

for x_0, ξ_0 that is directly proportional to the ΔT like for the introduced amount of heat quantity [6] . When the temperature of environment is T_e, where x_0 is directly proportional to the square root of heat spreading time t like for nonlinear diffusion case [1], we used relation $\Delta T / T_e$ for the temperature of environment T_e and the normal room temperature $T_S = 293.15\ K$ representing the constant source.

The obtained solutions of equation (9) are presented in Table 2. The experimental heat penetration depths can define thermal diffusion coefficients D_e with dimension $m^2 s^{-1}$. In this way, the dependence of $D_e T / T_e$ on temperature at constant pressure (2) p can be used. We can find a sufficiently exact solution of the system of equations (11), (12) and (13), when $a_4 = 0$ and the boundary condition (15) is as follows:

$$-a_3 \xi_0^3 + a_2 \xi_0^2 - a_1 \xi_0 = \frac{\Delta T}{T_e}\ ,\ \ \Delta T = T_S - T_e. \tag{19}$$

The sufficiently exact solutions $f(z)$ calculated by Mathcad 2013 are presented in Table 2 .

Table 2

The Dependence of Parameters a_1, a_2, a_3, ξ_0 for Approximate Solution $f(z)$ on $\Delta T / T_e$, when $T_S = 295{,}15\,K$

$t_e\,^0C$	$T_e\ K$	$\Delta T / T_e$	ξ_0	a_1	a_2	a_3	$\Delta T /(T_e \xi_0)$
17	290.15	0.0172	0.041	-0.422	-0.085	-0.0083	0.4195
7	280.15	0.0535	0.122	-0.449	-0.087	-0.0080	0.4385
-3	-270.15	0.0925	0.202	-0.477	-0.090	-0.0076	0.4579
-23	-250,15	0.180	0.360	-0.533	-0.094	-0.0070	0.500
-53	-220.15	0.3407	0.604	-0.622	-0.099	-0.0061	0.5641
-53	-220.15	0.3407	0.606	-0.623	-0.099	0.0000	

The profiles of functions f_i and F_i (14) like $(T(\xi) - T_e)/T_e$ for heat source temperature $T_S = 295.15\ K$ and the environment temperatures -3,-23 $t_e\,^0C$ and -23,-53 $T_e\,^0C$ are presented graphically using Mathcad 2013 in Fig. 1 and Fig. 2, respectively.

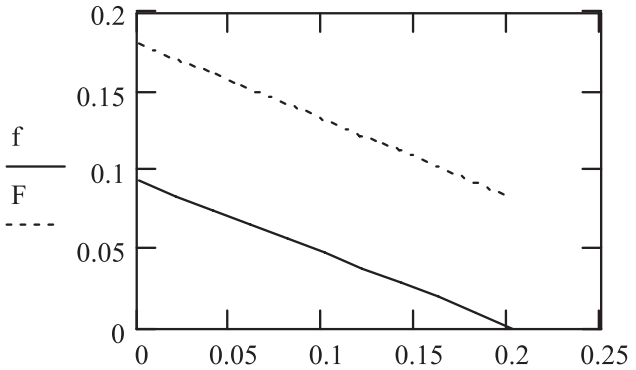

Fig. 1. Profiles of functions $f(z = \xi)$ and $F(z = \xi)$ presenting relative differences $(T(\xi) - T_e)/T_e$ of source $T_S = 295.15\ K$ and environment temperatures respectively $T_e =$ -3,-23 ^0C.

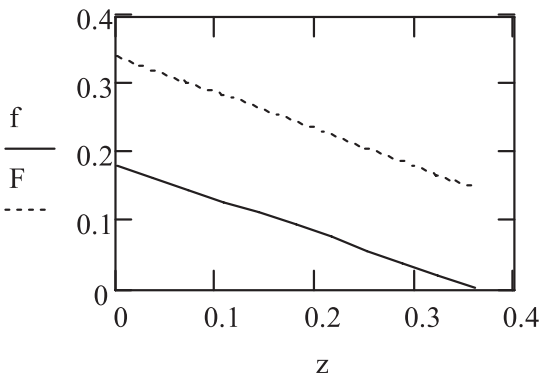

Fig. 2. Profiles of functions $f(z = \xi)$ and $F(z = \xi)$ representing relative differences $(T(\xi) - T_e)/T_e$ of source $T_S = 295.15\ K$ and environment temperatures respectively $t_e =$ -23, -53 ^0C.

The profiles in Fig. 1 and Fig. 2 are parallel lines, which are defined by $\Delta T/(T_e\xi_0)$ and relations

$$\Delta T/(T_e\xi_0) = C(T_S, T_e) \qquad (20)$$

presented by slowly changing numbers $C(T_S, T_e)$ in Table 2. The form of the obtained profiles approximately coincides with the profiles of nonlinear diffusion in solids when the diffusion coefficient is directly proportional to concentration of impurities for temperature depending on time [10]. The quantity of the heat Q_S introduced in gases from surface with square S can be equally transmitted to gasses

$$Q_S = K(T)\cdot S\frac{T_S - T_e}{x_0}t,\ Q_p = 0.5\cdot c_p\overline{\rho}V\Delta T = 0.5\cdot c_p\overline{\rho}\Delta S\cdot\Delta T\cdot x_0\ , \quad (21)$$

The obtained result is similar to the quantity of the introduced impurities by the nonlinear diffusion [11] when impurity concentration N_S at the crystal surface stays constant

$$Q = 0.5492N_S x_0\ . \qquad (22)$$

In the nonlinear thermodiffusion model, heat transition by the molecules with large $\Delta T/T_e$ and significantly greater average kinetic energy such as diffusion of some impurities in cold gases can be considered. The heat spreading from a point source with heat quantity Q in a one dimensional case in x axis is presented by changing of temperatures [12] and defined by $\sqrt{D_S t}$

$$T(x,t) - T_S(0,0) = \frac{Q}{\rho_l c\sqrt{\pi 4D_S t}}\exp(-x^2/4D_S t), \qquad (23)$$

at linear material density ρ_l with specific heat c. Here, as in (21) the transferred heat quantity Q from the point source at $x = 0$ is approximately proportional to square root of time at the distance $x < 2\sqrt{D_S t}$. This result is similar to the results obtained in [1] where linear diffusion profiles are small at the region $x \approx x_0$ for nonlinear diffusion.

4. RESULTS AND CONCLUSIONS

A similar task and approach have been considered for nonlinear diffusion [2], [13], [14] in gases. In this case, the definition of diffusion coefficients, which depend on average values of frequencies of molecule collisions in the frontier region of diffusion profiles, has been introduced. For practical calculations of temperature profiles, the coefficients a_1, a_2, a_3 at small $\Delta T/T_e = 0.02, 0.5, 0.1$ are sufficiently exact (19) and approximately coincide with coefficients of solution of nonlinear dif-

fusion equation [11]. For these values of $\Delta T / T_e$ the average meaning of $\overline{\nu}$ for approximate (2) $D_e T / T_e$ evaluation can be used. For definition of $D_e T / T_e$ value dependence on temperatures and pressures, the values a_1, a_2, a_3, presented in Table 2 at $\Delta T / T = 0.05$, can be used. By the convergence of the obtained values a_1, a_2, a_3 presented in Table 2, we get that for a case of maximum values $\Delta T /(T_e \xi_0)$ the constants a_1, a_2 practically coincide (19) when we take $a_3 = 0$. The results presented in Table 2 show that heat penetration depths x_0 and ξ_0 (17) are approximately proportional to $\Delta T / T_e$ values. In the case of nonlinear heat conductivity (4), we obtained like in the Fourier's law of heat conduction (21) that the transmitted heat quantity is proportional to ΔT. It is very important for practical applications of measured values $T(x \geq x_0) = T_e$, x_0, ΔT and analytical solutions (19) for definition of D_e. Using (21) Q_S we can find temperature of source T_S when measurements are hard, for example, walls and windows of buildings. Using (21) $x_0 = \xi_0 \sqrt{D_e t}$, D_e we can obtain

$$Q_S = \overline{K} \cdot S(T_S - T_e) \frac{x_0}{D_e \xi_0^{\,2}} \tag{24}$$

transmitted heat Q_S by surface S for definition of heat conductivity $\overline{K}$ from measurements ΔT, x_0, T_S, T_e, calculated (19) ξ_0 and Table 1.

REFERENCES

1. Janavičius, A.J. (1997). Method for solving the nonlinear diffusion equation. *Physics Letters A*, *224*, 159–162.
2. Janavičius, A.J., & Turskienė, S. (2016). Nonlinear thermal conductivity in gases. *Proc. of the Lithuanian Mathematical Society*, Ser. A, *57*, 21–28, DOI: 10.15388/LMR.A.2016.05
3. Janavičius, A.J., & Turskienė, *S.* (2006). Modeling of thermodiffusion inertia in metal films heated with ultrashort lasers pulses. *Acta Phys. Pol. A, 110*, 511–521.
4. Rudakov, V.I ., & Ovcharov V. V. (2001). Mathematical description of the diffusion a temperature field and measuring the heat of transport, *International Journal of Heat and Mass Transfer, 45*, 743–753.
5. Joos, G., & Freeman, I.M. (1986). *Theoretical physics.* New York: Dover Publications, Inc.
6. Janavičius, A.J., & Poškus, A. (2005). Nonlinear diffusion equation with diffusion coefficient directly proportional to concentration of impurities. *Acta Phys. Pol. A, 107*, 519–521.
7. Yu, J., Yang, Y., & Campo, A. (2010). Approximate solution of the nonlinear heat conduction equation in a semi-infinite domain. *Mathematical Problems in Engineering, 2010*, Article ID 421657. DOI:10.1155/*2010/421657.*
8. Filchakov, P. F. (1973). *Handbook of high mathematics*. Kiev: Scientific Thought (in Russian).
9. Goldin, L.L. (1983). *Laboratory works in physics*. Novosibirsk: Science (in Russian).

10. Janavičius, A.J. (1997). Nonlinear diffusion in excited systems. *Lithuania Journal of Physics, 37*(6), 508–510.
11. Janavičius, A.J. (1998). Nonlinear many-staged diffusion. *Acta Phys. Pol. A*, *93*, 731–735.
12. Knoibiul, F.K. (1981). *Handbook for repeating of physics*. Moscow: Energoizdat (in Russian).
13. Apostol, B.F. (1997). On a non-linear describing clouds and wreaths of smoke. *Phys. Lett. A*, *235*, 363–366.
14. Janavičius, A.J., Lūža G., & Jurgaitis, D. (2004). The nonlinear diffusion equation describing spread of impurities of high density. *Acta Phys. Pol. A*, *107*, 475–483.

NELINEĀRĀ TERMODIFŪZIJA GĀZĒS, ESOT VIDĒJĀM TEMPERATŪRĀM

A.J. Janavičius, S. Turskienė

K o p s a v i l k u m s

Rakstā tiek analizētas nelineārās termodifūzijas vienādojuma īpašības, kas apraksta difūzijas procesus, kuri notiek galīgā ātrumā. Agrākajos darbos prof. A. J. Janavičius ir piedāvājis nelineāro difūzijas vienādojumu ar difūzijas koeficientu, kas ir tieši proporcionāls piemaisījumu koncentrācijai. Šis vienādojums precīzāk raksturo *Si* kristālu piemaisījumu profilus.

Siltuma pārnese gāzēs var notikt ar lielāku vidējo kinētisko enerģiju, jo nelineārās difūzijas gāzes molekulas no karstām zonām nonāk aukstākās tāpēc, ka nejaušas Brauna daļiņas pārvietojas ar galīgu ātrumu. Šajā gadījumā siltumpārnese gāzēs var tikt aprakstīta ar nelineārās termodifūzijas vienādojumu, kur siltumpārneses un termodifūzijas koeficienti ir tieši proporcionāli temperatūrai *T*. Iegūtie aptuvenie nelineārās termodifūzijas vienādojuma atrisinājumi veiksmīgi tiek izmantoti, lai definētu temperatūras profilu un siltumpārneses koeficientu gāzē. Darba rezultāti liecina, ka siltuma izplatīšanās gāzēs ir atkarīga no temperatūru starpības un gāzes spiediena.

23.03.2018.

sciendo

LATVIAN JOURNAL OF PHYSICS
AND TECHNICAL SCIENCES
2018, N 3

DOI: 10.2478/lpts-2018-0020

SOLID STATE PHYSICS

FINDING ELECTRON-HOLE INTERACTION IN QUANTUM KINETIC FRAMEWORK

E. Klotins

Institute of Solid State Physics, University of Latvia,
8 Kengaraga Str., Riga, LV-1063, LATVIA
klotins@cfi.lu.lv

The article presents a quantum kinetic framework to study interacting quantum systems. Having the constituting model Hamiltonians of two-band semiconductor and the photoexcited electron-hole pair, their quantum kinetic evolution has been revisited. Solution to this nonlinear problem of electron-hole interaction is obtained making use of the self-consistency loop between the densities of photoexcited electrons and holes and the pairwise interaction terms in the constituting model Hamiltonians. In the leading order, this approach supports the required isomorphism between the pairwise interaction and the birth and annihilation operators of the photoexcited electrons and holes as a desirable property. The approach implies the Hilbert space and the tensor product mathematical techniques as an appropriate generalization of the noninteracting electron-hole pair toward several-body systems.

Keywords: *Hilbert spaces, photoexcited electron-hole pair, quantum electrodynamics*

1. INTRODUCTION

Quantum kinetic description of mater is a problem at the frontiers of condensed matter physics and constitutes the key challenge to the technological developments based on light-semiconductor interaction. This motivates for a renewed effort to develop a systematic framework for the electronic structure of interacting quantum systems in a manner going beyond the typical weak interaction approaches and available to complex many-body phenomena characterised by coexistence of the constituting particles and fields. Conventional quantum mechanics is successful in the case of particles, which simply propagate with no interactions. However, in the study of quantum many-body problems of realistic complexity the focus of attention is displaced from the one particle kinetics to multi-particle kinetics and gives rise to the quasiparticle solutions. The associated quantum kinetic model of the electron-hole pair is an important field of research and has been widely developed and extensively studied by V. N. Pervushin [1], S.A. Smolyansky [2] and collaborators [3]–[5].

The system found implicitly behind these models is a semiconductor at the temperature low enough to confine the charge carriers, the electron and the hole, to the impurities. The impurity concentration is presumably small and obeys conditions of the electron-hole symmetry. The set of parameters adapted in [1]–[5] and categorised here as the fundamental level constituents includes the effective mass of the electron and the hole, their charge, and the value of the main gap between the conduction and valence bands. This free field picture is perturbed by optical radiation appropriate for transition of an electron between the conduction and valence bands. The resulting quantum kinetics of the electron-hole pair obeys the special relativity and symmetry principles in a unitary and non-perturbative quantum description as an advantage.

By revisiting the electron-hole interaction problem, the aim of the present manuscript is to develop the approach of [1]–[5] toward the complex multi-particle systems in terms of interacting fundamental level constituents. In this regard, the manuscript provides an illustrative construction for the electron-hole pair as a compound system constituted of two subsystems, an electron and a hole, whose pairwise interaction comes into the game in time dependent electromagnetic radiation [1]. The required mathematical formalism includes the linear algebra [6] within the oscillator equation framework [7]–[10] as a promising and elegant formalism that relies heavily on the Hilbert spaces concept and underlies the observables of physical objects of interest. In more detail, our concern is the pairwise (Coulomb) interaction between the photoexcited electron and the hole. To proceed, we make use of the quantum electrodynamics [7]–[10] and the quantum kinetics [1], [11] framework.

The novelty, implemented in this framework firstly to the best of author's knowledge, is definition of the combined electron-hole system as the tensor product of the electron and hole states. Within the associated Hilbert space framework, the electron-hole pair comprising two particles (N=2) is found in accord with [3] as expected. Extensions toward N>2 for constructing quantum mechanical theories of several particle interacting Coulomb systems are available as a desirable property. Another novelty is the self-consistency conditions between the observables as the quantum kinetic result and the fundamental constituents of the constituting macroscopic Hamiltonians.

The physical picture of this framework include spatially homogeneous interacting spineless Coulomb systems under a spatially homogenous time-dependent electric field represented (at appropriate wavelength) by the electromagnetic vector potential in the Coulomb gauge.

The manuscript is organised as follows. Section 2 presents (i) the essential topics used in the prototypical non-interacting electron-hole pair model and (ii) the first steps towards a unifying framework for interacting extended quantum systems with interacting quantum constituents. Special attention is paid to the connection between the constituting macroscopic Hamiltonians and the associated Lagrangian density. Section 3 comprises a formal development of quantum field functions as a prerequisite for subsequent field-particle correspondence going beyond the usual application of wave functions. Special attention is paid to the symmetry and relativistic requirements that force the number of electron not to be conserved under time dependent optical radiation. Section 4 is addressed to the birth and annihilation of

electron-hole pairs in terms of the birth and annihilation operators with optical radiation and pairwise electron-hole interaction as key entities. Section 5 provides an abstract of the self-consistency loop connecting the quantum field and the quantum kinetic results. Section 6 concludes with a summary of the results and some remarks on future perspectives of other systems of interest.

2. BASIC CONCEPTS AND DEFINITION OF TERMS

The section provides a sketch of the elactron-hole pairwise interaction and the many-particle approaches. The constituting Hamiltonian is the following:

$$H = \frac{1}{2m}\left[\mathbf{p} - q\mathbf{A}\left(\mathbf{x},t\right)\right]^2 + V \ , \tag{1}$$

where q is the electric charge of a photoexcited particle with momentum $\mathbf{p}$ and $\mathbf{p2}/(2m)$ is regarded to its kinetic energy. In the Dirac's sea treatment, the charge for electron and hole is $q_e = -|e|$ and $q_h = +|e|$, respectively. The potential energy term V is the bandwidth, constituting the simplest model of an electron-hole pair [2]. The optical radiation involves a spatially homogenous time-dependent electric field represented by the vector potential $\mathbf{A}$ in the Coulomb gauge $\nabla \cdot \mathbf{A} = 0$. The electron-hole pair is categorised as a complex physical system where both the electron and the hole obey the time-independent free field Schrödinger equation. The physical picture involves the electron and the hole both contributing to the potential energy proportionally to their pairwise interaction.

From the perspective of interacting electron-hole pair, the key entities are basis vectors $\Psi_c(\mathbf{x},t)$ and $\Psi_v(\mathbf{x},t)$ that are elements of the state spaces S_c and S_v for the electron and the hole. We define the combined electron hole system as the tensor product:

$$S_{cv} = S_c \otimes S_v \, . \tag{2}$$

It means that for each pair of states $\Psi_c(\mathbf{x},t) \in S_c$ and $\Psi_v(\mathbf{x},t) \in S_v$ there is a combined state space $|\Psi_c, \Psi_v\rangle \equiv |\Psi_c\rangle \otimes |\Psi_v\rangle = |\Psi_c\rangle|\Psi_v\rangle \in S_{cv}$ where the hole is in valence state $|\Psi_v\rangle$ and the electron is in the conduction state of $|\Psi_c\rangle$. For the prototypical system of an electron and a hole, the requested tensor product of electron and hole states is the following:

$$\left[\hat{E}_c - \Delta/2 - \varepsilon_e(\hat{\mathbf{p}})\right] \otimes \left[\hat{E}_v + \Delta/2 + \varepsilon_h(\hat{\mathbf{p}})\right] \Psi_c \Psi_v = 0 \, . \tag{3}$$

A desirable property of the tensor product framework is its applicability to many-particle quantum systems formed in N single-particle spaces as $S^N = S_1 \otimes S_2 \otimes ... \otimes S_N$. However, the requirements for appropriate algebraic relations between the operators and the abstract Hilbert spaces must be extended by sev-

eral special features, including the restrictions of special relativity and the symmetry principles essential for constructing quantum kinetic theories of strongly interacting systems. As expected for two-particle systems, the tensor product (3) turns in the oscillator equation for the joint wave function:

$$\left[\hat{E}-\left(\Delta/2+W_c\right)-\varepsilon_c\left(\hat{\mathbf{P}}\right)\right]\left[\hat{E}+\left(\Delta/2+W_v\right)-\varepsilon_h\left(-\hat{\mathbf{P}}\right)\right]\Psi(\mathbf{x},t)=0\,, \tag{4}$$

where W_c, W_v specify the unknown yet impact of pairwise electron-hole interaction regarded to the potential energy in (1). The $\Psi(\mathbf{x},t)$ is the joint electron-hole state in (3) and the kinetic dispersion of the conduction and valence states are defined as $\varepsilon_c(\hat{\mathbf{P}})=\left(\hat{\mathbf{p}}^2+|e|\mathbf{A}\hat{\mathbf{p}}\right)/\left(2m_e\right)$, $\varepsilon_v(-\hat{\mathbf{P}})=\left(\hat{\mathbf{p}}^2-|e|\mathbf{A}\hat{\mathbf{p}}\right)/\left(2m_h\right)$.We express the energy operator $\hat{E}\to i\partial_t$ and the momentum operator $\hat{\mathbf{p}}\to -i\nabla$.

The Lagrangian density associated which the oscillator equation implies two complex conjugate field functions $\Psi\left(\mathbf{x},t\right)$ and $\Psi^*\left(\mathbf{x},t\right)$

$$L(\mathbf{x},t)=\frac{1}{\Delta}$$
$$\left(\begin{array}{l}\dfrac{\left(W_v-W_c-\varepsilon_c(\mathbf{P})+\varepsilon_v(-\mathbf{P})\right)^2}{4}\Psi\Psi^*-\dfrac{\left(W_c+W_v+\Delta+\varepsilon_c(\mathbf{P})+\varepsilon_v(-\mathbf{P})\right)^2}{4}\Psi\Psi^* \\ +\dfrac{i\left(W_v-W_c-\varepsilon_c(\mathbf{P})+\varepsilon_v(-\mathbf{P})\right)}{2}\left(\Psi^*\dot{\Psi}-\Psi\dot{\Psi}^*\right)+\dot{\Psi}^*\dot{\Psi}\end{array}\right), \tag{5}$$

where the factor $1/\Delta$ provides necessary dimension balance, and the kinetic dispersions are obtained by replacements $\varepsilon_c(\hat{\mathbf{P}})\leftrightarrow\varepsilon_c(\mathbf{P})$, $\varepsilon_v(-\hat{\mathbf{P}})\leftrightarrow\varepsilon_v(-\mathbf{P})$ valid in the case of quadratic isotropic dispersion. The Lagrangian density (5) and the field functions $\Psi\left(\mathbf{x},t\right)$ and $\Psi^*\left(\mathbf{x},t\right)$ are the starting points for the unitary part of the unified framework.

3. NORMALIZATION OF FIELD FUNCTIONS

In the present section, the Lorentz invariant, relativistic normalized and canonically quantized field functions are constructed. These special features imply four Fourier transformations:

$$\Psi(x)=\int d^4p\left(2\pi\right)^{-4}\tilde{\Psi}(p)\exp\left(-ipx\right) \tag{6}$$

$$\Psi^*(x)=\int d^4p\left(2\pi\right)^{-4}\tilde{\Psi}^*(p)\exp\left(ipx\right) \tag{7}$$

where properties of the system are implemented in the momentum space fields $\tilde{\Psi}(p)$ and $\tilde{\Psi}^*(p)$. The 4-vector scalar product $px=Et-\mathbf{px}$ is defined in $\{+,-,-,-\}$ metric signature.

To proceed to the momentum space fields, we make use of the integral from

to the generalized scaling property [3] as follows:

$$\int f(E,\mathbf{p})\delta\big(g(E,\mathbf{p})\big)dE = \sum_i f(E_i)/\left|g'(E_i)\right| . \tag{8}$$

here the $g(E,\mathbf{p})$ function and the field amplitudes $f(E,\mathbf{p})$ are defined as:

$$g(E,\mathbf{p}) = \left[E-\left(\Delta/2+W_c\right)-\varepsilon_c(\mathbf{P})\right]\left[E+\left(\Delta/2+W_v\right)+\varepsilon_v(-\mathbf{P})\right], \tag{9}$$

$$f(E,\mathbf{p}) = \psi(E,\mathbf{p})\exp(-iEt). \tag{10}$$

The field functions (6), (7) turn into

$$\Psi(\mathbf{x},t) = \int \frac{d\mathbf{p}}{(2\pi)^{3/2}} \left(\begin{array}{l} \left(\frac{1}{\sqrt{2\pi}}\right)\frac{1}{\Delta+W_c+W_v+\varepsilon_c(\mathbf{P})+\varepsilon_v(-\mathbf{P})} \\ \psi\left(\Delta/2+W_c+\varepsilon_c(\mathbf{P})\right)e^{-i\left(\Delta/2+W_c+\varepsilon_c(\mathbf{P})\right)t}+ \\ \psi\left(-\Delta/2-W_v-\varepsilon_v(-\mathbf{P})\right)e^{i\left(\Delta/2+W_v+\varepsilon_v(-\mathbf{P})\right)t} \end{array} \right) e^{i\mathbf{p}\mathbf{x}} . \tag{11}$$

Finally, the generalized scaling property (8) is obtained as a function of the macroscopic entities:

$$\begin{array}{l} \sum_i \frac{f(E_i,\mathbf{p})}{\left|g'(E_i)\right|} = \frac{1}{W_c+W_v+\Delta+\varepsilon_c(\mathbf{P})+\varepsilon_v(-\mathbf{P})} \\ \left\{ \begin{array}{l} \psi\left(\Delta/2+W_c+\varepsilon_c(\mathbf{P})\right)\exp\left[-i\left(\Delta/2+W_c+\varepsilon_c(\mathbf{P})\right)\right]+ \\ \psi\left(-\Delta/2-W_v+\varepsilon_v(-\mathbf{P})\right)\exp\left[i\left(\Delta/2+W_v+\varepsilon_v(-\mathbf{P})\right)\right] \end{array} \right\} . \end{array} \tag{12}$$

The direct field functions (6), (7) turn into

$$\Psi(\mathbf{x},t) = \int \frac{d\mathbf{p}}{(2\pi)^{3/2}} \left(\begin{array}{l} \left(\frac{1}{\sqrt{2\pi}}\right)\frac{1}{\Delta+W_c+W_v+\varepsilon_c(\mathbf{P})+\varepsilon_v(-\mathbf{P})} \\ \psi\left(\Delta/2+W_c+\varepsilon_c(\mathbf{P})\right)e^{-i\left(\Delta/2+W_c+\varepsilon_c(\mathbf{P})\right)t}+ \\ \psi\left(-\Delta/2-W_v-\varepsilon_v(-\mathbf{P})\right)e^{i\left(\Delta/2+W_v+\varepsilon_v(-\mathbf{P})\right)t} \end{array} \right) e^{i\mathbf{p}\mathbf{x}} \tag{13}$$

and the complex conjugate.

4. CANONICAL QUANTIZATION

As the first step toward the canonical quantization, we redefine the unknown yet ψ^- functions in (12) in time-independent creation-annihilation amplitudes $\psi\left(\Delta/2+W_c+\varepsilon_c(\mathbf{p})\right)=a_c(\mathbf{p})$, $\psi\left(-\Delta/2-W_v-\varepsilon_v(-\mathbf{p})\right)=a_v(-\mathbf{p})$ $\psi^*\left(\Delta/2+W_c+\right.$ $\left.+\varepsilon_c(\mathbf{p})\right)=a_c^*(\mathbf{p})$, $\psi^*\left(-\Delta/2-W_v-\varepsilon_v(-\mathbf{p})\right)=a_v^*(-\mathbf{p})$. The subsequent box normalization [13] that involves a box of volume L^3 allows replacing the integral representation of the field functions (13) by sums on the momentum space $\sum_{\mathbf{p}}(2\pi)^{3/2}L^{-3}->\int d^3\mathbf{p}(2\pi)^{-3/2}$. Another concern is redefinition of the creation-annihilation amplitudes $a(\mathbf{p})$ in operators $a_{\mathbf{P}}$ by relation $a(\mathbf{p})=\left(L/(2\pi)\right)^{3/2}a_{\mathbf{p}}$ [13].

Finally, the field functions (6), (7) harmonized with the constituting (reference) Hamiltonians are as follows:

$$\Psi(\mathbf{x},t)=\frac{1}{L^{3/2}}\sum_{\mathbf{p}}\left\{\begin{array}{c}\dfrac{\sqrt{\Delta}}{\sqrt{\left(W_c+W_v+\Delta+\varepsilon_c(\mathbf{P})+\varepsilon_v(-\mathbf{P})\right)}}\\ \left[a_e(\mathbf{p})e^{-i\left(W_c+\Delta/2+\varepsilon_c(\mathbf{P})\right)t}+a_h(-\mathbf{p})e^{i\left(W_v+\Delta/2+\varepsilon_v(-\mathbf{P})\right)t}\right]e^{i\mathbf{px}}\end{array}\right\}, \tag{14}$$

$$\Psi^*(\mathbf{x},t)=\frac{1}{L^{3/2}}\sum_{\mathbf{p}}\left\{\begin{array}{c}\dfrac{\sqrt{\Delta}}{\sqrt{\left(W_c+W_v+\Delta+\varepsilon_c(\mathbf{P})+\varepsilon_v(-\mathbf{P})\right)}}\\ \left[a_e^\dagger(\mathbf{p})e^{+i\left(W_c+\Delta/2+\varepsilon_c(\mathbf{P})\right)t}+a_h^\dagger(-\mathbf{p})e^{-i\left(W_v+\Delta/2+\varepsilon_v(-\mathbf{P})\right)t}\right]e^{-i\mathbf{px}}\end{array}\right\}. \tag{15}$$

The structure of field functions (14), (15) is in accord with [2] obtained by the decomposition of the (unknown yet) wave function into the superposition of plane waves corresponding to electron and hole.

A complementary to (14), (15) approach is developed in [5], which differs in minor details and is not considered in the present manuscript.

Having the field functions and the Lagrangian density (5) the canonical momenta $\pi=\partial L/\partial\dot{\Psi}$ is as follows:

$$\pi(\mathbf{x},t)=\frac{i}{\sqrt{\Delta}}\sum_{\mathbf{p}}\left\{\begin{array}{c}\dfrac{\sqrt{W_c-W_v+\Delta+\varepsilon_c(\mathbf{P})+\varepsilon_v(-\mathbf{P})}}{2L^{3/2}}\\ \left(e^{it\left(W_c+\Delta/2+\varepsilon_c(\mathbf{P})\right)}a_c^\dagger(\mathbf{p})-e^{-it\left(W_v+\Delta/2+\varepsilon_v(-\mathbf{P})\right)}a_v^\dagger(-\mathbf{p})\right)e^{-i\,\mathbf{xp}}\end{array}\right\} \tag{16}$$

$$\pi^*(\mathbf{x},t)=\frac{-i}{\sqrt{\Delta}}\sum_{\mathbf{p}}\left\{\begin{array}{c}\dfrac{\sqrt{W_c+W_v+\Delta+\varepsilon_c(\mathbf{P})+\varepsilon_v(-\mathbf{P})}}{2L^{3/2}}\\ \left(e^{-it\left(W_c+\Delta/2+\varepsilon_c(\mathbf{P})\right)}a_c^+(\mathbf{p})-e^{it\left(W_v+\Delta/2+\varepsilon_v(-\mathbf{P})\right)}a_v^+(-\mathbf{p})\right)e^{i\,\mathbf{xp}}\end{array}\right\}. \tag{17}$$

Another derived quantity, the Hamiltonian density, obeys the relation

$$H = \pi \dot{\Psi} + \pi^* \dot{\Psi}^* - L(\Psi). \tag{18}$$

In lowest order approximation [3], accepted in the manuscript, the last term in (18) is discarded without loss of generality. Then the total Hamiltonian is as follows:

$$H_{tot} = \frac{1}{2L^3} \sum_{\mathbf{p}} \begin{pmatrix} (W_c + \Delta/2 + \varepsilon_c(\mathbf{p})) a_c(\mathbf{p}) a_c^\dagger(\mathbf{p}) + \\ (W_v + \Delta/2 + \varepsilon_v(-\mathbf{p})) a_v(-\mathbf{p}) a_v^\dagger(-\mathbf{p}) \end{pmatrix}, \tag{19}$$

where the pairwise interaction is supported by the non-relaxed photoexcited charges after the optical radiation is switched off.

At the next level of approximation, the kinetic momentum is maintained and the creation-annihilation operators become time-dependent as obtained by replacements $\varepsilon_{c,v}(\pm\mathbf{p}) -> \varepsilon_{c,v}(\pm\mathbf{P})$ and $a_{c,v}(\pm\mathbf{p}) -> a_{c,v}(\pm\mathbf{P},t)$. Then the total Hamiltonian (19) turns in the quasiparticle representation:

$$H_{tot}(t) = \frac{i}{2L^3} \begin{pmatrix} a_{e,\mathbf{p}}^\dagger(t) \dot{a}_{e,\mathbf{p}}(t) - a_{h,-\mathbf{p}}^\dagger(t) \dot{a}_{e,\mathbf{p}}(t) + a_{e,\mathbf{p}}^\dagger(t) \dot{a}_{h,-\mathbf{p}}(t) - a_{h,-\mathbf{p}}^\dagger(t) \dot{a}_{h,-\mathbf{p}}(t) \\ -a_{h,-\mathbf{p}}(t) a_{e,\mathbf{p}}^\dagger(t) \lambda(\mathbf{p},t) + a_{e,\mathbf{p}}(t) a_{h,-\mathbf{p}}^\dagger(t) \lambda(\mathbf{p},t) - a_{e,\mathbf{p}}(t) \dot{a}_{e,\mathbf{p}}^\dagger(t) + \\ a_{h,-\mathbf{p}}(t) \dot{a}_{e,\mathbf{p}}^\dagger(t) - a_{e,\mathbf{p}}(t) \dot{a}_{h,-\mathbf{p}}^\dagger(t) + a_{h,-\mathbf{p}}(t) \dot{a}_{h,-\mathbf{p}}^\dagger(t) \end{pmatrix}, \tag{20}$$

where $\lambda(\mathbf{p},t) = \dot{\Omega}(\mathbf{p},t) / \Omega(\mathbf{p},t)$ and $\Omega(\mathbf{p},t) = \sqrt{W_c + W_v + \Delta + \varepsilon_c(\mathbf{P}) + \varepsilon_v(-\mathbf{P})}$.

The equations of motion for the birth and annihilation operators follow from the minimal action principle:

$$S = \int d^4x \left\{ \pi \dot{\Psi} + \pi^* \dot{\Psi}^* - H_{tot}(t) \right\} \tag{21}$$

The operator equations of motion follows after functional derivation which respect to the field amplitudes

$$\dot{a}_{e,\mathbf{p}}(t) = \frac{\lambda(\mathbf{p},t)}{2} a_{h,-\mathbf{p}}(t) - i a_{e,\mathbf{p}}(t) \left(W_c + \frac{\Delta}{2} + \varepsilon_c(\mathbf{p},t) \right) \tag{22}$$

$$\dot{a}_{e,\mathbf{p}}^\dagger(t) = \frac{\lambda(\mathbf{p},t)}{2} a_{h,-\mathbf{p}}^\dagger(t) + i a_{e,\mathbf{p}}^\dagger(t) \left(W_c + \frac{\Delta}{2} + \varepsilon_c(\mathbf{p},t) \right) \tag{23}$$

$$\dot{a}_{h,-\mathbf{p}}(t) = \frac{\lambda(\mathbf{p},t)}{2} a_{e,\mathbf{p}}(t) + i a_{h,-\mathbf{p}}(t) \left(W_v + \frac{\Delta}{2} + \varepsilon_v(\mathbf{p},t) \right) \tag{24}$$

$$\dot{a}^{\dagger}_{h,-\mathbf{p}}(t)=\frac{\lambda(\mathbf{p},t)}{2}a^{\dagger}_{e,\mathbf{p}}(t)-ia^{\dagger}_{h,-\mathbf{p}}(t)\left(W_{v}+\frac{\Delta}{2}+\varepsilon_{v}(\mathbf{p},t)\right) \tag{25}$$

Here the field amplitudes are redefined by replacements $a(\mathbf{p},t)\to a_{\mathbf{p}}(t)$, and the band indices v/c (valence/conduction) are replaced by quasiparticle indices h/e. The first terms in (22)–(25) describe creation and annihilation of the electron-hole pairs with the amplitude of interband transitions $\lambda(\mathbf{p},t)$ under action of the optical radiation. The pairvise interaction is condensed in the amplitude of interband transitions (20) and in the last terms written here as the algebraic representation of the Heisenberg commutator $i\left[H,a(\mathbf{p},t)\right]$ [2]. The set of equations (22)–(25) concludes the quantum unitary evolution stage and is appropriate for making contacts with the adiabatic quantum Vlasov description [11].

5. FROM QUANTUM UNITARY EVOLUTION TO IRREVERSIBLE QUANTUM VLASOV DESCRIPTION

Kinetic description of the electron-hole pairs is based on the distribution function formalism well accepted in problems of the particle pair production from the vacuum in strong time-dependent laser radiation [11], [7]. For the electron and the hole distribution functions in quasiparticle representation, we follow [2]:

$$f_{e,h}(\mathbf{p},t)=\left\langle 0_{in}\left|a^{\dagger}_{e,h,\mathbf{p}}(t)a_{e,h,\mathbf{p}}(\mathbf{p},t)\right|0_{in}\right\rangle, \tag{26}$$

$$f_{h}(-\mathbf{p},t)=\left\langle 0_{in}\left|a^{\dagger}_{h,-\mathbf{p}}(t)a_{h,-\mathbf{p}}(t)\right|0_{in}\right\rangle \tag{27}$$

where the charge conservation implies as $f_{e}(\mathbf{p},t)=f_{h}(-\mathbf{p},t)$. The quantum Vlasov equations for the fermion distribution functions [1], [2] are as follows:

$$\dot{f}_{e,h}(\mathbf{p},t)=\lambda(\mathbf{p},t)\int_{-\infty}^{t}dt'\lambda(\mathbf{p},t')\left[1-2f_{e,h}(\mathbf{p},t')\right]\cos\left(2\theta(\mathbf{p},t,t')\right), \tag{28}$$

where the alternating phase $\theta(\mathbf{p},t,t')=\int_{t'}^{t}d\tau[\varepsilon(\mathbf{P}(\tau))+\Delta/2]$. While the amplitude of the interband transitions follows the applied field instantly, the non-Markovian behaviour is maintained, and the kinetics is adiabatic. The connection between the quantum unitary evolution and the distribution function formalism utilizes a selfconsistent collective field created by electrons and holes that depends in a complex way on the distribution functions. The available extensions involve the tensor product framework (3) and the pairwise interaction managed by recursive application of the time-dependent photoexcited particle number density in the adiabatic particle number basis:

$$n(t) \equiv \int d\mathbf{p}\, f(\mathbf{p},t) \tag{29}$$

and of the Coulomb interaction treated in the non-relativistic limit:

$$W \equiv -\frac{e^2 n(t)}{4\pi\varepsilon_0 \left[\mathbf{r}_e - \mathbf{r}_h\right]} \quad . \tag{30}$$

Then, finally, the expected self-consistency loop holds between the densities of photoexcited electrons and holes (29), the pairwise interaction (30) and the Hamiltonian (20) where the effective electron-hole distance emerges as a parameter.

6. CONCLUSIONS

Based on the Schrödinger type constituting Hamiltonians of two-band semiconductor and the existence of the photoexcited electron-hole pair, we have reconsidered their (first order) interaction in terms of the quantum unitary and the adiabatic Vlasov description. Although not unique, this model involves the prototypical electron-hole pair as a compound system constituted of two subsystems, an electron and a hole, which obeys the special relativity and symmetry principles crucial for quantum mechanical theories of strongly interacting particles.

This implies the Hilbert space of the compound electron-hole system as tensor product of the constituting subsystems, the electron and the hole, as most appropriate generalization of the prototypical electron-hole pair toward several body systems characterised by coexistence of the constituting particles and fields.

The novelty, addressed to bypass the mathematical difficulties inherent in the pairwise (electron-hole) interaction (30) is the self-consistency loop that connects the phoexcited particle number density (29) and the quasiparticle representation obtained as a quantum kinetic result (20). In the leading order, this novelty provides the required isomorphism between the pairwise interaction and the birth and annihilation operators of the photoexcited electrons and holes.

Although the present manuscript has demonstrated the quantum unitary evolution and the adiabatic Vlasov description for the distribution function of a single interacting electron-hole pair, an insight into other situations of interest is possible such as quantized electromagnetic radiation, half-integer spins and the crystal field models that are the areas of further research.

ACKNOWLEDGEMENTS

The present research has been supported by the Institute of Solid State Physics, the University of Latvia within the framework of National Research Program IMIS2. [Grant numbers VPPI IMIS2, IMIS4].

REFERENCES

1. Pervushin, V.N., Skokov, V.V., Reichel, A.V., Smolyansky, S.A., & Prozorkevich, A.V. (2005). The kinetic description of vacuum particle creation in the oscillator representation. *Int. J. Mod. Phys*. *A20*, 5689–5704. https://doi.org/10.1142/S0217751X05028909
2. Smolyansky, S.A., Tarakanov, A.V., & Bonitz, M. (2009). Vacuum particle creation: analogy with the Bloch theory in solid state physics. *Contrib. Plasma Phys*., *49*, 575–584. DOI 10.1002/ctpp.2009 10058S
3. Smolyansky, S.A., Bonitz, M., & Tarakanov, A.V. (2010). Strong field generalization of the interband transitions kinetics. *Physics of Particles and Nuclei*, *41*, 1075–11078. DOI 10.1134/S106377961007021X
4. Pervushin, V.N., & Skokov, V.V. (2006). Kinetic description of fermion production in the oscillator representation. *Acta Physica Polonica B, 37*, 2587–2600.
5. Friesen, A.V., Prozorkevich, A.V., Smolyansky, S.A., & Bonitz, M. (2007). Nonperturbative kinetics of electron-hole excitations in strong electric field. *Proc. SPIE 6537, Laser Physics and Photonics, Spectroscopy and Molecular Modeling V II*, 653701. doi:10.1117/12.754724
6. Von Neumann, J. *(1932/1996). Mathematical foundations of quantum mechanics, Princeton landmarks in mathematics. Princeton University Press.* ISBN 978-0-691-02893-4*,* MR 1435976
7. Fedotov, A.M., Gelfer, E.G., Korolev, K.Yu., & Smolyansky, S.A. (2011). Kinetic equation approach to pair production by a time-dependent electric field. *Physical Review D*, *83*(2), id. 025011. DOI:10.1103/PhysRevD.83.025011
8. Grib A.A., Mamaev, S.G., & Mostepanenko, V.M. (1994). *Vacuum quantum effects in strong fields* [in Russian], Energoatomizdat, M. (1988); English transl., Friedmann Laboratory Publishing, St. Petersburg (1994).
9. Schmidt, S. M., Blaschke, D., Röpke, G., Smolyansky, S.A., Prozorkevich A.V., & Toneev, V.D. (1998). A quantum kinetic equation for particle production in the Schwinger mechanism. *Int. J. Mod. Phys., E7*, 709–722. https://doi.org/10.1142/S0218301398000403
10. Schmidt, S.M., Blaschke, D., Röpke, G., Prozorkevich, A.V., Smolyansky, S.A., & Toneev V.D. (1999). Non-Markovian effects in strong-field pair creation. *Phys. Rev. D59*, 094005.
11. Blaschke, D.B., Smolyansky, S.A., Panferov, A., & Juchnowski, L. (2017). Particle production in strong time-dependent fields. arXiv:1704.04147v1 [hep-ph] 28 Mar 2017.
12. Álvarez-Gaumé, L., & Vázques-Mozo, M.Á. (2012). An invitation to quantum field theory. Lecture Notes in Physics 839. DOI:10.1007/978-3-642-23728-7_2, Berlin: Springer Verlag.
13. Schwabl, F. (2005). *Advanced quantum mechanics*. Berlin: Springer Verlag.

ELEKTRONU-CAURUMU MIJIEDARBĪBA KVANTU-KINĒTISKĀ APRAKSTĀ

E. Klotiņš

K o p s a v i l k u m s

Raksts veltīts mijiedarbojošos kvantu sistēmu studijām divu zonu pusvadītāja modelī, kas ietver elektronu un caurumu sistēmu, pakļautu pāru tipa mijiedarbībai. Attiecīgais nelineārais uzdevums atrisināts izveidojot pašsaistes cilpu, kura noslēdzas izmantojot unitāru kvantu kinētiku fotoierosināto elektronu un caurumu skaitliskā blīvuma aprakstam un Vlasova vienādojumu neatgriezeniska elektrona-cauruma pāra mijiedarbības makroskopiskam aprakstam. Rezultāts pirmā tuvinājumā nodrošina nepieciešamo izomorfismu starp pāra mijiedarbību un elektrona-cauruma dzimšanas un anihilācijas operatoriem. Aprēķinos ilustrētais Hilberta telpas un tenzoru reizinājuma matemātiskais formālisms ir vispiemērotākais prototipisko divu daļiņu apraksta paplašināšanai vairākdaļiņu sistēmām un tā pielietojums, iespējams, arī citās nozīmīgās situācijās, saistītās ar kvantētu elektromagnētisko starojumu, pus-veseliem spiniem un kristāla lauka modeļiem.

25.03.2018.

sciendo

LATVIAN JOURNAL OF PHYSICS
AND TECHNICAL SCIENCES
2018, N 3

DOI: 10.2478/lpts-2018-0021

STUDY OF THE OPERATIONAL PROPERTIES OF BISTABLE SMECTIC-A LIQUID CRYSTAL DISPLAYS

M. Maltisovs [1, 2], K. Krumins [1], A. Ozols [1], D. Pikulins [2]

[1]EuroLCDs Ltd., VATP-2, Ventspils, LV-3602, LATVIA
E-mail: matiss.maltisovs @gmail.com
[2]Institute of Radioelectronics, Riga Technical University,
12 Azenes Str., Riga, LV-1048, LATVIA

Nowadays liquid crystal display (LCD) is an integral part of humans' everyday life. High demand for new and innovative LCD products force LCD industry to develop and implement new types of LCDs. Bistable smectic-A (SmA) LCD is one of the most promising devices for smart glass applications due to long-term bistability, low haze at clear state, low transmittance at scatter state and low power consumption.

The study describes the most relevant conclusions obtained from frequency response testing and electric current measurements of bistable SmA LCD samples. Bistable LCDs have two states: opaque (light scattering state) and focal conic (transparent state). Switching between clear and scatter states and vice versa is a frequency dependant process. The conducted research on bistable SmA LC frequency response provides important knowledge about operation principles of the smart glass devices.

Keywords: *bistable, frequency response, liquid crystal displays, smart glass, smectic-A*

1. INTRODUCTION

Smart or switchable glass is glass with voltage dependant optical properties, which can be altered if specific electrical signals are applied to the glass. The main advantages of smart glass are the following:

- privacy – a fast state change from clear to scattering state and vice versa, low transmittance in opaque state, ability to replace curtains, shutter blinds, drapes;
- cost savings – no need for additional cleaning equipment, saving costs for heating, air-conditioning and lighting, avoiding the costs of installing and maintaining motorized light screens, blinds or curtains;
- UV protection – blocks > 98 % of UV rays;

- display and advertising – can be used as a projection screen when switched to the scatter state.

Smart glass technologies include electrochromic, suspended particle and polymer dispersed liquid crystal (PDLC) devices. Each of these types has different working principles, advantages, and disadvantages.

Electrochromic smart glass is the most popular – currently it utilizes an electrochromic film with an ion storage layer and ion conductor placed between two transparent sheets. An electric potential initiates a redox reaction of the electrochromic film transitioning the colour and the transparency of the smart glass [1].

Suspended particle smart glass has needle shaped particles suspended within an organic gel placed between two electrodes. In its off state (scattered), the particles are randomly dispersed and have low light transmittance. Once a voltage is applied, the needle particles will orient themselves to allow for light to pass through [1].

PDLC smart glass works similarly to the suspended particle variety. However, in PDLC smart glass, the central layer is a liquid crystal placed within a polymer matrix between electrodes. Similar in behaviour to the suspended particles, in the off (scattering) state the liquid crystals are randomly dispersed and have low light transmittance. When voltage is applied and an electric field is created, the liquid crystals orient themselves allowing light to pass through. PDLC film appears milky white due to the refractive index mismatch encountered by incoming light at the liquid crystal/polymer interface [1].

Bistable SmA liquid crystal displays differ from the above mentioned with lower power consumption due to the need for an electric field only during switching between states [2], [3]. For example, PDLC, Electrochromic and Suspended particle smart glass devices need an electric field to sustain one or both states, but bistable devices can sustain both states due to very high LC viscosity. SmA LC formulation also offers better optical properties (< 87 % transmittance in the transparent state and < 1.7 % in the scattering state) than PDLC (< 41 % transmittance in the transparent state and < 23 % in the scattering state) [4].

Existing studies do not provide detailed information on bistable SmA LC operational properties [5], [6]. Contrary to a majority of studies that have been conducted using small samples <50x50mm, the present research is based on 300x400mm large bistable SmA LC devices. The main goal is to determine the most suitable frequencies for switching the bistable LCDs to transparent and scattering states, i.e., frequencies that provide the highest light transmittance at the transparent state and the lowest light transmittance at the scattering state, taking into account the switching speed.

2. EXPERIMENTAL PART

A total of three different experimental series have been performed. For these experiments, two different types of bistable SmA LCDs have been manufactured. Both types have 300x400mm outer dimensions and active area equally divided into 8 pixels (one pixel is 95x275mm), which can be switched individually or as a single

unit if they are connected in parallel [7], [8]. To maintain a constant cell gap, 15 μm plastic ball spacers with density of 10 pcs/mm^2 have been used. LC has been supplied by Dow Corning Corporation [9], [10]. The main difference between the two LCD types used for these experiments lies in the dielectric (isolation) coating application procedure: for half of the devices the dielectric coating Silicon dioxide (SiO_2) has been applied before Indium tin oxide (ITO) ablation process and for other half – dielectric coating has been applied after ITO ablation. Contacts have been soldered on top and bottom electrodes (see Figs. 1, 2).

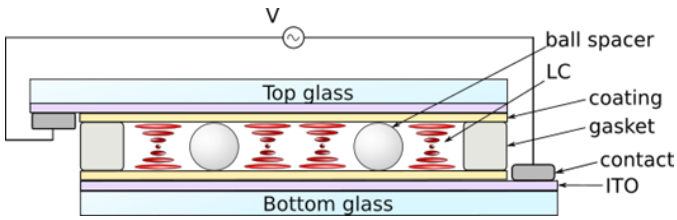

Fig. 1. Schematic picture of LC cell: cross-section [11].

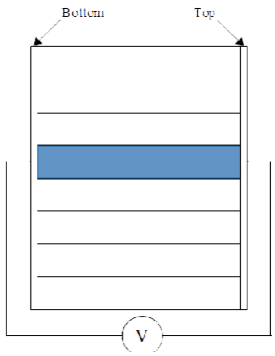

Fig. 2. Schematic picture of LC cell – top view.

Three samples from each display type have been used in these experiments. The first experiment has been devoted to obtaining the frequency response of LC cell. The reference frequencies – 1 kHz frequency for switching to the transparent state and 50 Hz frequency for switching to the scattering state – have been chosen on the basis of the LC manufacturer's recommendations. The operating voltage 13V/μm has been determined in other experiments. Experimental setup, shown in Fig. 3, consists of:

- alternating high-voltage (AHV) source, which provides a necessary voltage level for creating an electric field to switch the samples;
- optical measurement platform (OPMP), allowing the measurements of light transmission and switching speed;
- white LED, used as a light source, photodiode VTB-1013BH with maximized response through the visible part of the spectrum utilised as light detector;
- Ocean Optics laboratory-grade optical fibre patch cords as light guides.

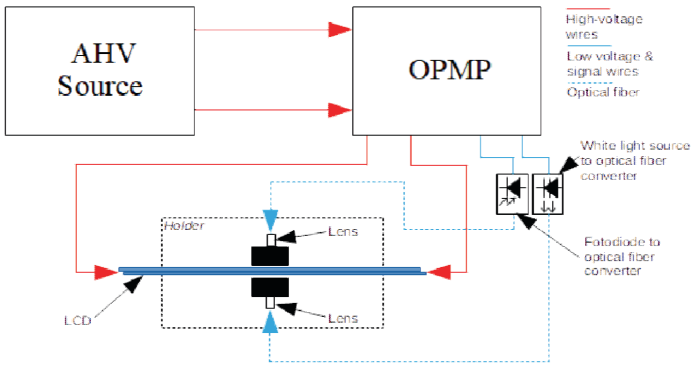

Fig. 3. Simplified schematic of frequency response measurement setup.

The second and third experiments have been carried out to obtain data on the most important electrical parameters of bistable SmA LCDs.

The data on optimised switching frequencies for both states obtained within the first experiment have been used to switch differently sized display areas of the LCD samples and measure voltage on the LCD and consumed electric power for a full display area, 1/2, 1/4 and 1/8 of the display area. Experimental setup for the second and third experiments is depicted in Fig. 4. Difference between both experiments is in additional external resistors, which are used to limit the display current during the third experiment. For the current limitation, 10 different external metal oxide film resistors with resistances ranging from 8.2 Ohm to 330 Ohm (according to the E24 standard) have been used. This experiment has allowed determining the minimal required current for fully switching display from the transparent state to the scattering state and vice versa. The fourth test series have been conducted in order to compare the data from the second experiment to the voltage and consumed power measurements obtained for the SmA LC manufacturer's recommended frequencies.

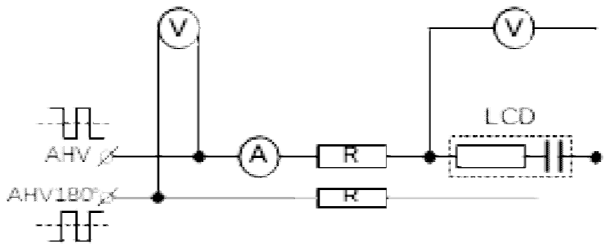

Fig. 4. Experimental setup for display current limitation and measurement.

3. RESULTS AND DISCUSSION

The dependence of driving frequency on light transmittance of bistable SmA LCD is shown in Fig. 5. The blue curve represents switching from the transparent to scattering state and the orange curve – switching from the scattering to trans-

parent state. Frequency range for switching to the scattering state is very narrow (10 Hz–60 Hz) compared to the frequency range for switching to the transparent state (200 Hz–1.5 kHz). The peak transmittance for switching to the transparent state can be obtained only in the frequency range between 500 Hz and 1 kHz.

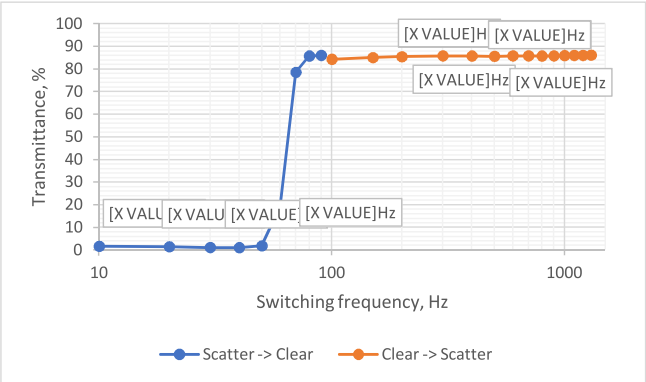

Fig. 5. Light transmittance at different driving frequencies.

More detailed graph showing the frequency range for switching to the scattering state, incorporating another important design parameter – switching speed (see orange curve), is shown in Fig. 6. It can be seen that the lowest switching speed and light transmittance can be achieved in the frequency range between 20 Hz–30 Hz.

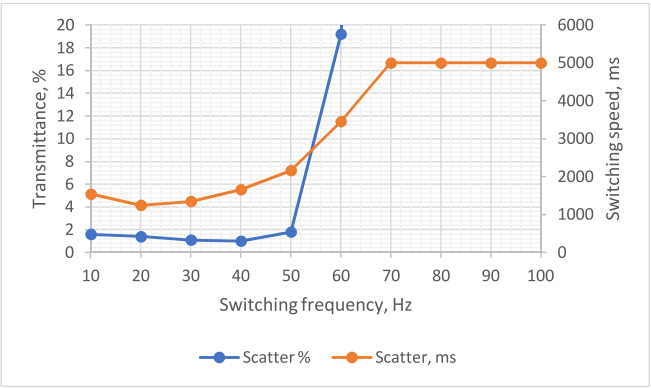

Fig. 6. Switching speed (orange) and light transmittance (blue) at different driving frequencies during transition to the scattering state.

The corresponding detailed graph showing the frequency range for switching to the transparent state is demonstrated in Fig 7. Light transmittance (blue) remains relatively constant (about 86 %) across most of the driving frequencies and switching speed (orange) reaches the lowest points around 116 ms–120 ms at the frequency range between 400 Hz and 700 Hz. Thus, this region could be the most suitable for switching to the transparent state.

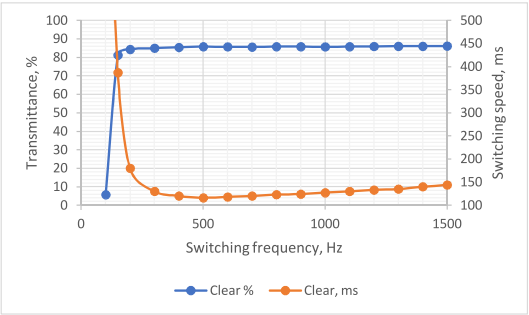

Fig. 7. Switching speed (orange) and light transmittance (blue) at different driving frequencies during transition to the scattering state.

During the second and third experiments, the consumed RMS current for differently sized display areas has been measured. The size of the switchable display area has been adjusted by connecting adjacent pixels in parallel. From the obtained data, the consumed RMS power has been calculated for all six tested displays, which is shown in Fig. 8. The power consumption increases exponentially depending on the number of pixels being used. The largest power consumption can be observed during transition to the transparent state when the whole display area is switched.

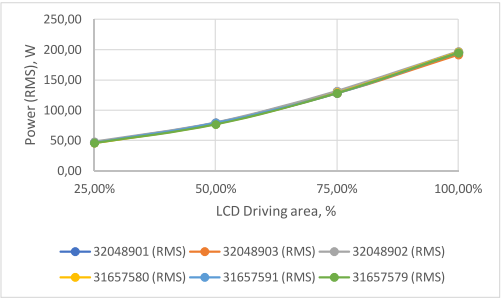

Fig. 8. Consumed RMS power depending on the size of the switched display area.

Current measurements with additional current limiting resistors for unit 32048903 (randomly chosen due to the obtained data similarity) are shown in Fig. 9. On the basis of the obtained results, it can be concluded that it is necessary to provide LCD with at least 0.9 A driving current to switch the whole display area from the scattering to transparent state and obtain > 85 % light transmission.

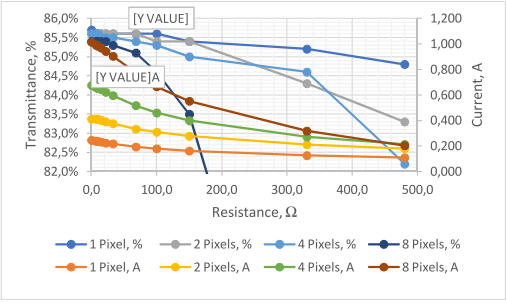

Fig. 9. Units 32048903 current measurements with current limiting resistors.

Additional power consumption measurements have been performed with 50Hz/1kHz and 30Hz/600Hz frequencies. Comparison between 600 Hz and 1 kHz can be seen in Table 1, between 30 Hz and 50 Hz in Table 2. Significant improvements can be obtained in RMS current and RMS power by changing frequencies for both switching states.

Table 1

Consumed Power Comparison between 600 Hz and 1 kHz

Driving frequency	Voltage	Peak current	RMS current	Peak power	RMS power	Transmittance
600 Hz	190 V	3.12 A	1.03 A	588.21 W	194.42 W	85.1 %
1 kHz	190 V	3.14 A	1.33 A	590.74 W	249.94 W	85.0 %
	Improvement:	0 %	22 %	0 %	22 %	

Table 2

Consumed Power Comparison between 30Hz and 50Hz

Driving frequency	Voltage	Peak current	RMS current	Peak power	RMS power	Transmittance
30 Hz	190 V	3.10 A	0.26 A	581.13 W	49.29 W	1.5 %
50 Hz	190 V	3.09 A	0.29 A	579.92 W	55.05 W	1.7 %
	Improvement:	0 %	10 %	0 %	10 %	

4. CONCLUSIONS

The experimentally obtained operation parameters of large size 300x400 mm bistable smectic-A liquid crystal display samples have been presented in the paper.

Frequency response studies show that reducing the driving frequencies for transition to both the transparent state and the scattering state gives significant improvements in power consumption of the bistable devices. Reducing the driving frequency from 1 kHz to 600 Hz (for transition to the transparent state) reduces the RMS current by 22 %, but reducing the driving frequency from 50 Hz to 30 Hz (for transition to the scattering state) reduces the power consumption by 10 %. In addition to power savings, the switching speed for both states has also improved, i.e., switching speed from the transparent to scattering state decreased from ~2100 ms to ~1300 ms (48 %), from the scattering to transparent state – from ~127 ms to ~118 ms (7 %).

Power measurements for 1px, 2px, 4px and 8px give information about correlation between power consumption and the size of the drivable display area and opportunity to predict power consumption for new LCD patterning designs. The obtained RMS power consumption increases exponentially, i.e., 2px (25 % of display area) consumed power is ~48W, 4px (50 %) ~80W, 6px (75 %) ~130W and 8px (100 %) ~198W.

By gradually limiting the switching current, it has been concluded that switching the whole LCD area from the scattering state to the transparent state requires at least 170W RMS power and at least 25W to switch only 1px. The highest power consumption can be observed during transition from the scattering to transparent

state due to high switching frequency; therefore, it is very important to investigate the behaviour of liquid crystal within its operating frequency range.

Further research will be focused on additional experiments with bistable smectic-A liquid crystal displays due to unknown behaviour in long-term functionality, including experiments with different coating materials, long-term switching tests to understand degradation boundaries for LC and LCD, driving experiments where LCDs are connected in series with one AHV power source, etc.

REFERENCES

1. Wong, K. V., & Chan, R. (2013). Smart glass and its potential in energy savings. *Journal of Energy Resources Technology*, *136*(1), 12002. https://doi.org/10.1115/1.4024768
2. Goodby, J. W., Collings, P. J., Kato, T., Tschierske, C., Gleeson, H. F., & Raynes, P. (2014b). *Handbook of liquid crystals. Volume 2: Physical properties and phase behavior of liquid crystals*. Boschstr. 12, 69469 Weinheim, Germany: Wiley-VCH Verlag & Co. KGaA. Available at https://www.wiley.com/en-lv/Handbook+of+Liquid+Crystals%2C+8+Volume+Set%2C+2nd+Edition-p-9783527327737
3. Goodby, J. W., Collings, P. J., Kato, T., Tschierske, C., Gleeson, H. F., & Raynes, P. (2014a). *Handbook of liquid crystals. Volume 8: Applications of liquid crystals*. Germany: Wiley-VCH Verlag & Co. KGaA. Available at https://www.wiley.com/en-lv/Handbook+of+Liquid+Crystals%2C+8+Volume+Set%2C+2nd+Edition-p-9783527327737
4. Ghosh, A., & Mallick, T. K. (2018). Evaluation of optical properties and protection factors of a PDLC switchable glazing for low energy building integration. *Solar Energy Materials and Solar Cells*, *176*, 391–396. https://doi.org/10.1016/j.solmat.2017.10.026
5. Coates, D., Crossland, W. A., Morrisy, J. H., & Needham, B. (1978). Electrically induced scattering textures in smectic a phases and their electrical reversal. *Journal of Physics D: Applied Physics*, *11*(14), 2025–2034. https://doi.org/10.1088/0022-3727/11/14/012
6. Gardiner, D. J., & Coles, H. J. (2007). Enhancing lifetime in a bistable smectic A liquid crystal device. *Journal of Physics D: Applied Physics*, *40*(4), 977–981. https://doi.org/10.1088/0022-3727/40/4/009
7. Lueder, E. (2010). *Liquid crystal displays: Addressing schemes and electro-optical effects* (2nd ed.). UK: John Wiley and Sons, Ltd. Available at https://www.wiley.com/en-lv/Liquid+Crystal+Displays%3A+Addressing+Schemes+and+Electro+Optical+Effects%2C+2nd+Edition-p-9780470688182
8. Cristaldi, D. J. R., Pennisi, S., & Pulvirenti, F. (2009). *Liquid crystal display drivers: Techniques and circuits* (1st ed.). Springer Science+Business Media B.V. https://doi.org/10.1007/978-90-481-2255-4
9. Hannington, J. P., Clapp, T. V., Nishida, F., King, R. K., Farooq, O., Grassman, M., … Pivnenko, M. (2013). *Oligosiloxane modified liquid crystal formulations and devices using same*. European patent.
10. Clapp, T. V., Crossland, W. A., Davey, A. B., Grassman, M., Hannington, J. P., King, R. K., … Xu, H. (2011). *Liquid crystal formulations and structures for smectic A optical devices*. Patent. Available at http://www.dowcorning.com/content/paintink/paintinkresin/default.aspx
11. Mozolevskis, G., Ozols, A., Nitiss, E., Linina, E., Tokmakov, A., & Rutkis, M. (2015). Reduction of electric breakdown voltage in lc switching shutters. *Latvian Journal of Physics and Technical Sciences*, *52*(5), 47–57. https://doi.org/10.1515/lpts-2015-0028

BISTABILO SMECTIC-A ŠĶIDRO KRISTĀLU DISPLEJU DARBĪBAS PARAMETRU IZPĒTE

M. Maltisovs, K. Krūmiņš, A. Ozols, D. Pikuļins

K o p s a v i l k u m s

Cilvēku ikdiena bez šķidro kristālu displeju (LCD) tehnoloģijām nav iedomājama. Augstais pieprasījums pēc jauniem un inovatīviem LCD produktiem piespiež industriju izstrādāt un ieviest jaunus LCD modeļus. Bistabilie Smectic-A (SmA) LCD ir viena no daudzsološākajām tehnoloģijām gudro stiklu produktu izstrādei, pateicoties ilgstošai bistabilitātei, augstai gaismas caurlaidībai caurspīdīgā stāvoklī, zemai gaismas caurlaidībai gaismu izkliedējošā stāvoklī un zemajiem energoresursu patēriņiem.

Bistabilo SmA LCD pārslēgšanās starp izkliedējošu (ieslēgtu) un caurspīdīgu (izslēgtu) stāvokli notiek ar dažādu frekvenču palīdzību. Pētījuma ietvaros tika veikti frekvenču, gaismas caurlaidības un pārslēgšanās ātruma mērījumi, efektīvāko pārslēgšanās frekvenču diapazonu noteikšanai. Displeja patērētās strāvas mērījumi izmantojot un neizmantojot papildus strāvu ierobežojošas pretestības, minimālās un maksimālās displeja patērētās jaudas noteikšanai. Izdarīti secinājumi par iegūtajiem rezultātiem, izteikti priekšlikumi turpmākajiem pētījumiem.

26.03.2018.

sciendo

LATVIAN JOURNAL OF PHYSICS
AND TECHNICAL SCIENCES
2018, N 3

DOI: 10.2478/lpts-2018-0022

ELECTRONIC COMMUNICATION

MATHEMATICAL ALGORITHM FOR PROCESSING MEASUREMENT RESULTS OF INTERNET ACCESS SERVICE IN THE SCOPE OF NET NEUTRALITY

I. Smirnova, E. Lipenbergs, V. Bobrovs

Department of Telecommunications, Riga Technical University,
1 Kalku Str., Riga, LV-1658, LATVIA
inga.smirnova@sprk.gov.lv

Since Regulation (EU) 2015/2120 of the European Parliament and of the Council came into force, Internet service providers have to fulfill various additional requirements in order to guarantee access to the open internet and provide transparent information to the end-users. Of the utmost importance is to ensure achievable, meaningful and comparable results of the internet quality indicators, particularly upload and download speed values. Regulation (EU) 2015/2120 stipulates that specific speeds should be indicated in the contracts: for fixed internet access service those are maximum, minimum, normally available and advertised speed and for mobile internet access service – estimated maximum and advertised speed. However, there are no common methods put in place to calculate required speed indicators that can lead to a large amount of noncomparable and unreviewable information and create difficulties for internet providers to describe quality indicators. Within the framework of the present research, a mathematical estimation algorithm has been elaborated and applied in order to ensure that required quality parameters are represented objectively and that they are intercomparable among different internet service providers. Unified calculation principle would foster end-user awareness of the meaning of quality indicators and also of the quality of received internet services. It would also facilitate the indication of the required information for internet service providers.

Keywords: *internet access service, net neutrality, quality of service*

1. INTRODUCTION

It is important to find a golden mean between user awareness and internet providers' ability to always ensure once indicated quality. What if sometimes a speed value is lower than specified minimum, or does not correspond to normally available, or it is several megabits per second lower than indicated maximum? Where is the borderline of acceptable noncompliance; and in which cases can an end-user take

advantage of some little discrepancy? Wouldn't it force internet providers to specify lower quality indicators just in case? And wouldn't it in the end badly influence internet providers' businesses and give incomprehensible information to the end-users. The aim of the present research is to find an objective and equitable method for calculating the required speed values and implementing measurement processing algorithm that would be optimised for specific technology but at the same time would give the most comparable result and would be unified as much as possible in order to represent comparable data among various internet providers [6].

To compare quality parameter values among different internet service providers, as well as provide meaningful information to the end-users and reflect a realistic situation, some mathematical calculations should be implemented.

2. PRACTICAL MEASUREMENTS

To examine the best interpretation of speed parameter weight and find out the most unified approach in value acquisition, measurements have been conducted both for mobile and for fixed internet access services. Measurements have been performed during twenty-four hours in a one-week period. The frequency of the measurements has been approximately ten minutes [4], [5]. Though the Regulation does not require mobile internet service providers to indicate minimum and normally available speed values [2], [3], in the present research it has been assumed as a necessity to broaden end-users' understanding of common and possible minimum speed values.

Within the framework of the research, various speed tests have been performed in different types of internet networks; they all have shown a correlation between speed values during the day and internet technology (e.g., ADSL technology has stable but low speed values, Fiber – rather stable and high, Mobile – rather unstable that varies from low to high). In the research, measurements of two types of internet technologies have been studied: FTTH *(Fiber to the Home*) and 4G *(fourth generation)* mobile.

A. Fixed Internet Measurements

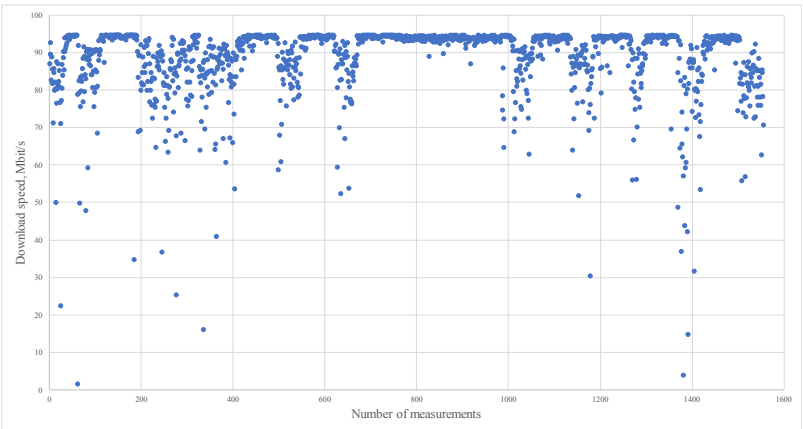

Fig. 1. Scatterplot of download speed distribution during the measurement period in the fixed network.

Analysing measurement results of fixed internet access service, the stability of speed can be observed. Speed fluctuations mostly appear during peak hours, although the drop of the speed is not significant. Only few measurements show values that are lower than 60 Mbits/s. The advertised maximum speed of this fixed internet test connection is 100 Mbits/s.

B. Mobile Internet Measurements

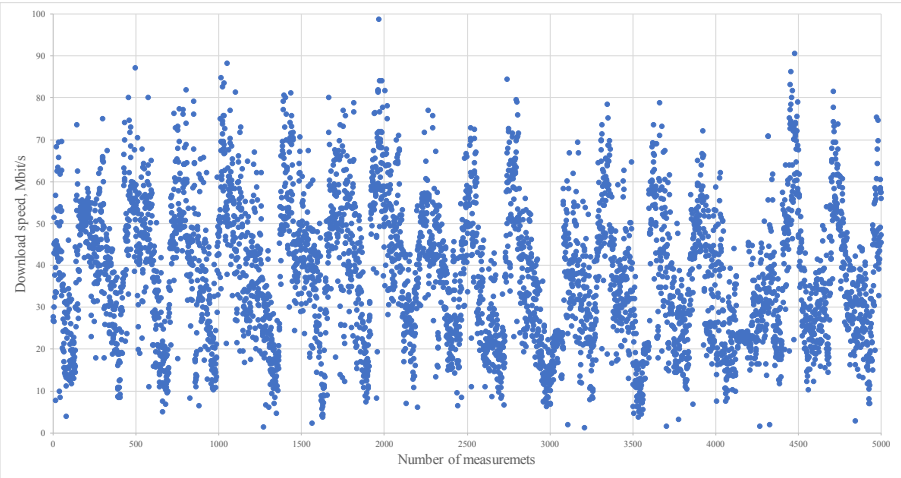

Fig. 2. Scatterplot of download speed distribution during the measurement period in the mobile network.

Analysing measurement results of mobile internet access service, it can be observed that speed is unstable during the day: it increases and decreases depending on the time of the day and varies from low to high in a wide range.

Quasiperiodicity of the download speed variation both in fixed and mobile networks can be explained by the end user's activity on the internet. Download speed lowers during the peak hours, particularly during the second half of the day and in the evenings when many end-users use the internet. Figures 1 and 2 show the download speed value of each measurement and represent the dynamics of its variation in time.

Although fixed and mobile internet speed values differ a lot, to give a comprehensible information to the end users and obtain a unified calculation approach for internet providers, it has been decided to apply a uniform calculation method both for fixed and for mobile internet access services.

3. CALCULATION OF THE SPEED VALUES

To observe the speed value distribution during the day, histograms have been made. These histograms show how often specific speed values occur during the day. The difference between the fixed and mobile internet is evident; they also have a non-normal distribution. Analysing the obtained results and evaluating the required

target, it can be stated that although value distribution differs, the common calculation methods can be applied.

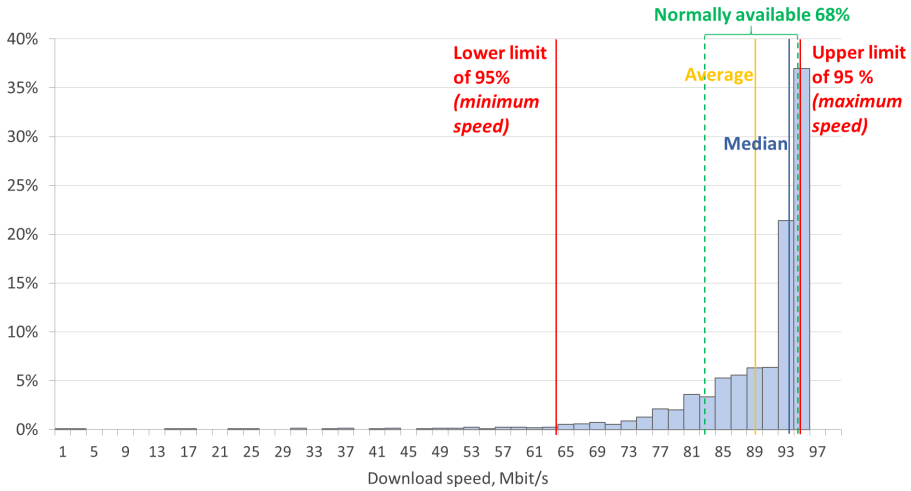

Fig. 3. Histogram of download speed values during the day in the fixed network.

The calculated download speed indicators of fixed internet access service are shown in Table 1.

Table 1

Download Speed Values of the Fixed Internet

Maximum	Minimum	Lower limit of 95 %	Upper limit of 95 %	Average	Median	Standard deviation	Average + standard deviation	Average - standard deviation	Lower limit of 68 %	Upper limit of 68 %
94.68	1.62	94.64	63.95	88.91	93.42	9.65	98.57	79.26	94.47	82.56

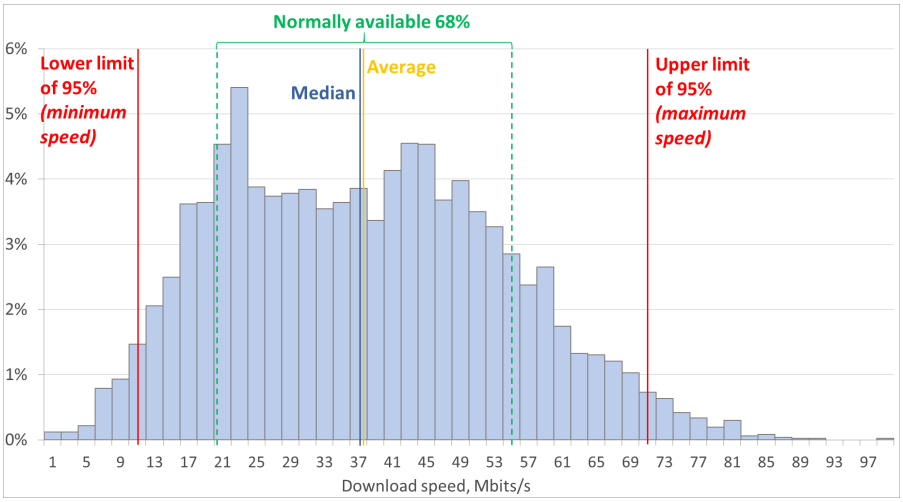

Fig. 4. Histogram of download speed values during the day in the mobile network.

The calculated download speed indicators of mobile internet access service are shown in Table 2.

Table 2

Download Speed Values of the Mobile Internet

Maximum	Minimum	Lower limit of 95 %	Upper limit of 95 %	Average	Median	Standard deviation	Average + standard deviation	Average - standard deviation	Lower limit of 68 %	Upper limit of 68 %
98.66	1.17	70.96	10.61	37.69	37.15	16.44	54.13	21.25	54.85	20.32

To avoid influence of some random values that occur rarely and do not reflect the overall situation, some confidence threshold should be determined. Fixed internet measurement results show that a majority of speed values are situated near the maximum value, whereas measured minimum values are distributed in the wide value range. Though they might occur, it happens rarely and does not influence the provided quality of service. Analogous situation takes place with the mobile internet; though the values are distributed in a wider range, the lowest and highest values occur rarely; thus, they do not give a realistic view on a minimum and maximum value. Therefore, to describe a realistic situation, it is advised to define a lower limit of value that would indicate an objective minimum value.

Analysing measurement results, it can be observed that values outside 95 % of measurements appear most rarely; therefore, to discard non-common values and avoid their influence on the result it is advised to cut 2.5 % values of the highest and lowest measurement values.

Figure 3 shows that in the fixed internet an average download speed value differs from median, and though more than a half of measurements (58 %) are in the range of 94 Mbit/s to 96 Mbit/s, the other half (42 %) are widely distributed with lower values.

On the contrary, in the mobile internet (Fig. 4) an average speed value and median are almost the same, but quite a large number of values are higher than the average; thus, for an end-user it does not give an overall notion of speed values that can be achieved during the use of the internet access service.

Taking it into account, some more descriptive methods to indicate normally available speed should be established rather than determining only one speed value. In the present research, it has been decided to indicate normally available speed in the speed range. Normally available speed should be achievable sufficiently often during the day. However, one should consider a reasonable deviation from the indicated value that can occur at specific times of the day, e.g., at peak hours, during congestions etc. To determine an adequate proportion when defining normally available speed values, some mathematical algorithms should be put in place. In the research, it has been decided to apply an empirical rule to the distribution of speed values in order to establish the most unified approach that would be applicable for different internet access technologies. The empirical rule states that in normal distribution 68 % of values are situated in the range of one standard deviation [1]. For the reason that measured speed distributions might differ from a normal distribution (as

observed during the research, see Figs. 3 and 4) as well to facilitate calculations for internet service providers and implement a unified calculation approach, instead of calculation of standard deviation, it has been suggested to generalise the calculations and estimate 68 % of values that are evenly distributed approximately around average value. For this reason, 16 % of the range of the highest and lowest measurement values has been cut. Thereby it is considered that normally available speed is a speed that is distributed in 68 % range of measurements performed during the day.

4. CONCLUSION

Determining the unified approach among internet providers gives a possibility to compare them and better understand the quality indicators. Due to the differences in technologies and achievable quality values, it is impossible to apply a completely universal approach. However, to get the information on realistic quality indicators and raise users' awareness of speed values they can achieve, a unified calculation algorithm should be implemented. The unified approach will serve as a method to gain comparable data, thus giving to public the meaningful information on different internet service providers. Indication of a normally available speed in the range gives a better insight of achievable speed values. It also provides flexibility to internet service providers to describe speed indicators, as well as safeguards them from end-users misusing a noncompliance with the indicated value that can sometimes occur by withdrawing from contract or claiming for indemnification. Representing normally available speed in the range gives end-users an understanding that the internet speed depends on several factors and normally available speed can vary in time.

REFERENCES

1. Peck, R., & Devore, J.L. (2011). *Statistics: The exploration and analysis of data* (7th ed.). USA: Brooks/Cole, ISBN: 978-0-8400-5801-0.
2. REGULATION (EU) 2015/2120 OF THE EUROPEAN PARLIAMENT AND OF THE COUNCIL of 25 November 2015 laying down measures concerning open internet access and amending Directive 2002/22/EC on universal service and users' rights relating to electronic communications networks and services and Regulation (EU) No 531/2012 on roaming on public mobile communications networks within the Union.
3. BEREC Guidelines on the Implementation by National Regulators of European Net Neutrality Rules BoR (16) 127, August 2016.
4. Stafecka, A., Lipenbergs, E., Bobrovs, V., & Sharashidze, T. (2017). Quality of service methodology for the development of internet broadband infrastructure of mobile access networks. In *IEEE Conference Proceedings* (pp.1–5), 19–21June 2017, Palanga, Lithuania, Kaunas: Kaunas University of Technology. ISBN 978-1-5386-0394-9.
5. Lipenbergs, E., Bobrovs, V., & Ivanovs, G. (2016). Investigation of service quality of measurement reference points for the internet services on mobile networks. *Latvian Journal of Physics and Technical Sciences*, *53*(5), 64–73. ISSN 0868-8257.
6. Lipenbergs, E., Bobrovs, V., & Ivanovs, G. (2016). Quality of service measurements references investigation for the mobile internet services in the context of net neutrality framework. In *Proceedings of 2016 Progress in Electromagnetics Research Symposium (PIERS 2016 Shanghai)* (pp.4248–4252), 8–11August 2016, Shanghai, China. Piscataway: IEEE. ISBN 978-1-5090-6094-8. e-ISBN 978-1-5090-6093-1.

INTERNETA PIEKĻUVES PAKALPOJUMA MĒRĪJUMU REZULTĀTU APSTRĀDES MATEMĀTISKAIS ALGORITMS TĪKLA NEITRALITĀTES JOMĀ.

I.Smirnova, E.Lipenbergs, V.Bobrovs

K o p s a v i l k u m s

Kopš Eiropas Parlamenta un Padomes Regula (ES) 2015/2120 stājās spēkā, interneta pakalpojuma sniedzējiem jāievēro vairākas papildu prasības, lai nodrošinātu piekļuvi atvērtam internetam un sniegtu galalietotājiem caurskatāmu informāciju. Visbūtiskākais ir sniegt jēgpilnu un salīdzināmu informāciju par sasniedzamiem interneta kvalitātes rādītājiem, jo īpaši par lejupielādes un augšupielādes ātrumiem. Regula (ES) 2015/2120 nosaka, kādus pieslēguma ātruma rādītājus interneta pakalpojuma sniedzējiem ir jānorāda līgumos ar galalietotāju, t.i.: fiksētam interneta piekļuves pakalpojumam jānorāda maksimālais, minimālais, parasti pieejamais un reklamētais ātrums, savukārt mobilam interneta piekļuves pakalpojumam – paredzamais maksimālais un reklamētais ātrums. Tomēr kopējas metodes ātrumu rādītāju aprēķinam nav noteiktas, līdz ar to, iespējams, radot nepārskatāmas un nesalīdzināmas informācijas daudzumu, kā arī radot grūtības interneta pakalpojuma sniedzējiem atspoguļot kvalitātes rādītājus. Pētījumā tika atrasts un piemērots matemātisks aprēķinu algoritms, ar kura palīdzību norādāmās lejupielādes ātruma kvalitātes vērtības būtu objektīvi atspoguļotas un savstarpēji salīdzināmas starp dažādiem pakalpojuma sniedzējiem. Vienots aprēķinu princips veicinātu lietotāju izpratni par vērtību nozīmi un saņemtā pakalpojuma kvalitāti, kā arī atvieglotu interneta pakalpojuma sniedzējiem minētās informācijas norādīšanu.

16.02.2018.

sciendo

LATVIAN JOURNAL OF PHYSICS
AND TECHNICAL SCIENCES
2018, N 3

DOI: 10.2478/lpts-2018-0023

SYNCHRONIZATION OF NON-LINEAR DYNAMIC SYSTEMS UNDER THE CONDITIONS OF NOISE ACTION IN THE CHANNEL

O. Golevych[1], O. Pyvovar[2], P. Dumenko[3]

[1&3] DiGas Ltd.
31 Talsu soseja, K-17-34, Jurmala, LV-2016, LATVIA
e-mail[1]: oleg_plus@mail.ru
e-mail[3]: p.dumenko@digasgroup.com
[2] Khmelnytskyi National University
11 Instytutska Str., 29016, Khmelnytskyi, UKRAINE
e-mail: opyvovar2@gmail.com

Areas of optimal amplitudes and minimal spectral unevenness of Rucklidge chaotic signals with better correlation abilities are demonstrated in the present research. A model of chaotic synchronization and information transmission system is implemented. The effect of the synchronization feedback coefficient and signal-to-noise ratio on the systems noise immunity is shown.

Keywords: *chaos, non-uniformity of the signal spectrum, Rucklidge, SNR, spectrum width, synchronization*

1. INTRODUCTION

Due to telecommunication systems development and radio frequency loading, as well as along with the need to ensure high speed and interference immunity, much attention is paid to the investigation of signal-code structures based on deterministic chaos signals. Signals of deterministic chaos have specific features that make it possible to separate them into a separate group of signals that are extremely promising in the role of channel subcarriers: broadband; complexity; orthogonality.

Ideally, the synchronization of deterministic chaos oscillators (DCG) [1]-[4] implies the simultaneity and uniformity of the evolution of the phase trajectories of spatially separated nonlinear dynamic system (NDS), a similar type of synchronization is called complete. The most common is a one-way synchronization type from the master oscillator to the slave. Investigations of bi-directional synchronization lead to unpredictable results as a result of competition between two modes of chaotic fluctuations.

If the structure of the associated NDS oscillators is the same, but there is some difference between the control parameters of the slave and master systems, by selecting other parameters and characteristics it is possible to provide a deterministic

relationship between the phase trajectories of the leading and slave oscillators. This similar synchronization type is called generalized.

2. DYNAMIC SYSTEM SELECTION AND ITS PARAMETER ANALYSIS

2.1 Dynamic Systems Evaluation Criteria

NDS of a certain structure can generate signals of different types, if it is possible to receive chaotic oscillations and such NDS describe some real process, then the oscillator gets its own name. Each such DCG has a range of values of initial conditions and control parameters that allow receiving signals of deterministic chaos.

To separate the input values of the dynamic system, in which only chaotic signals are generated, it is necessary to prove the linear independence of the group consisting of a series of realizations of the chaotic signal taken at different time intervals, i.e., to calculate their mutual correlation characteristics [5]. Due to the non-periodicity of the chaotic signal, the realizations form a linearly independent basis. In an ideal case, implementations in a group must be pairwise orthogonal.

Based on the results of the analysis [6], [7] for the construction of a communication system, it is advisable to use the Rucklidge NDS, whose signals in the majority of estimates have better spectral and correlation properties than other NDS.

2.2 Rucklidge Oscillator Signal Statistics

Rucklidge oscillator is described with a system of three nonlinear differential equations [8]. The results of the distribution analysis of the gramian G values [6] and the spectral nonuniformity ΔN_s from the values of the control parameters K and L (Fig. 1) make it possible to isolate the range of generation parameters of the deterministic chaos, which is extremely wide for this oscillator, that allows varying the parameters during the construction of a chaotic telecommunication system.

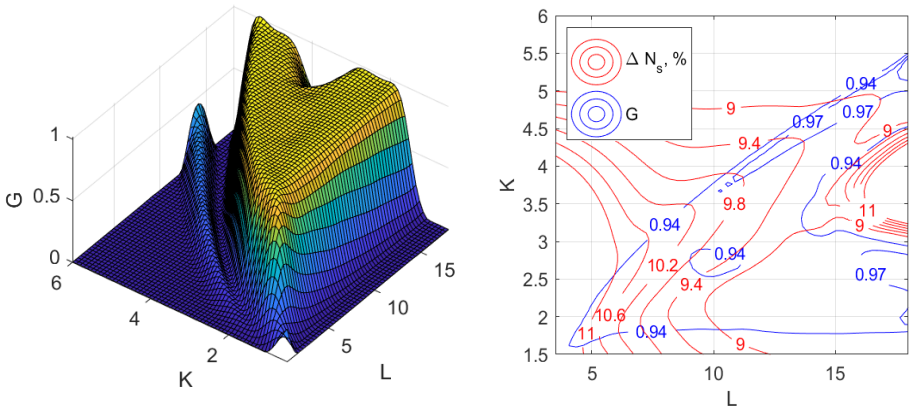

Fig. 1. Distribution gramian values (G) (left) and distribution of the gramian values G and spectral nonuniformity values ΔN_s (right).

In order to find the regions of the parameters of the incoming values of K and L at which the Rucklidge system generates chaotic signals with a high degree of orthogonality and minimal spectrum unevenness, a criterion was used according to which values of K and L the determinant of the Gram matrix composed of DCS realizations would be above 0.9 (full range gramian distribution shown in Fig. 1).

Choice of the control parameters K and L in order to ensure the stealthiness of the digital communication system being developed with chaotic subcarriers should be made in such a way as to ensure the maximum similarity of the parameters and characteristics of the signals in the transmission line.

3. TELECOMMUNICATION SYSTEM USING GENERALIZED SYNCHRONIZATION

3.1 Research Problem

In the construction of telecommunication systems based on chaos oscillators, there are a number of problems that complicate their practical implementation and synchronization, including:

- high sensitivity of secondary system parameters to the accuracy and stability of composite elements;
- the need to use chaotic synchronization and chaotic synchronous response to ensure the correct operation of the system on the receiving and transmitting side of the communication line;
- the nature of the interference effect on chaotic communication systems is significantly different from the interference effect on linear systems.

To solve the research problems, modelling is reasonable to be carried out in the aspects of determining the optimal values of the NDS control parameters and their synchronization system under the condition of interference.

3.2 The Principle of Transmitting Digital Signals Using NDS

Under the conditions of a digital modulating message, the most acceptable method for practical implementation is the method of receiving chaotic signals, based on the use of parallel auxiliary NDS. The essence of the method consists in the introduction parallel to the receiving unit on the basis of a chaotic oscillator of an additional block identical in structure.

The essence of digital level transmission in the described system of two slave oscillators and one master oscillator is to introduce a unidirectional connection from the master oscillator to the slaves of such a level that it would be possible to capture the chaotic behaviour of the master oscillator by the slaves under given initial conditions. The transition from chaotic synchronization of slave oscillators to desynchronization should have a pronounced threshold for the possibility of effectively separating the logical levels of the digital information message. After the “capture” of the behaviour of the driven oscillators, regardless of the differences their parameters,

the difference between the state vectors of the driven chaotic oscillators is minimal.

On the contrary, in the case of setting the driving parameters of the master oscillator in the desynchronization zone, the master oscillator is not capable of "imposing" its chaotic mode to the slave. As a result of this fact, each of the slaves operates autonomously and, owing to chaotic behaviour, their phase trajectories exponentially spread out, which leads to a large difference between their state vectors. Thus, the digital modulation of the control parameter values makes it possible to transmit two digital levels using the presence and absence of generalized synchronization between chaotic pairs of the master-slave oscillator.

Such a logic level transfer scheme eliminates the problem of a high initial identity of the control pairs of the parameters between the slave and the master oscillators that are spaced apart in space.

Unidirectional communication between slave and master oscillators is introduced by means of a nonreciprocal adder of two channels with a total unit transmission coefficient (1). The first channel provides internal communication over one of the possible state variables of the oscillator with a transmission coefficient b, where $0 < b < 1$, the second channel provides transmission of a synchronizing signal from the master oscillator with a coefficient transfer of $(1-b)$. Only such a way, at provided complete identity of all oscillators, the difference between their state vectors is zero.

The fact of the presence or absence of generalized synchronization during the transmission of a certain digital level is fixed by analysing the differences in the state vectors of the slave oscillators. Such an analysis can be conducted according to different criteria, the most popular of which is the mean square error of reception in the transmission interval of one bit. The differences in the reception error between the signals of the two slave oscillators during the logical zero and the logical one transmission determine the reception margin when identifying logical levels, which in turn determines the noise immunity of the system as a whole.

3.3 Transmission System Model

The mathematical model of the system of three connected Rucklidge oscillators, which are the basis of a chaotic communication system, based on the principle of identifying chaotic synchronization with the help of an auxiliary NDS, is as follows:

$$\begin{cases} \frac{dx_{m1}}{dt} = -K_{m1} \cdot x_{m1} + L_{m1} \cdot y_{m1} - y_{m1} \cdot z; \ \frac{dy_{m1}}{dt} = x_{m1}; \ \frac{dz_{m1}}{dt} = -z + {y_{m1}}^2; \\ \frac{dx_{s1}}{dt} = -K_{s1} \cdot x_{s1} + L_{s1} \cdot (y_{m1} \cdot (1-b) + y_{s1} \cdot b) - (y_{m1} \cdot (1-b) + y_{s1} \cdot b) \cdot z_{s1}; \\ \frac{dy_{s1}}{dt} = x_{s1}; \frac{dz_{s1}}{dt} = -z_{s1} + (y_{m1} \cdot (1-b) + y_{s1} \cdot b)^2; \\ \frac{dx_{s2}}{dt} = -K_{s2} \cdot x_{s2} + L_{s2} \cdot (y_{m1} \cdot (1-b) + y_{s2} \cdot b) - (y_{m1} \cdot (1-b) + y_{s2} \cdot b) \cdot z_{s2}; \\ \frac{dy_{s2}}{dt} = x_{s2}; \ \frac{dz_{s2}}{dt} = -z_{s2} + (y_{m1} \cdot (1-b) + y_{s2} \cdot b)^2, \end{cases} \quad (1)$$

where x_{m1}, y_{m1}, z_{m1} – the state vector (phase coordinates) of the master oscillator;
x_{s1}, y_{s1}, z_{s1} – the state vector of the main slave oscillator;
x_{s2}, y_{s2}, z_{s2} – the state vector of the auxiliary slave oscillator.

As criteria for identifying the presence of generalized synchronization between chaotic oscillators, two different similarity criteria were used during the simulation.

The standard deviation criterion δ_1 and criterion of the average rectified deviation δ_2 are often used to determine the reception error in analogue communication systems:

$$\delta_1 = \frac{1}{N}\sum_{i=1}^{N}\left(u_i - v_i\right)^2 \quad ; \quad \delta_2 = \frac{1}{N}\sum_{i=1}^{N}\left|u_i - v_i\right|, \tag{2}$$

where u_i, v_i – phase coordinates of the main and additional slave oscillator, respectively; N – the sample size taken for analysis.

$$\Delta_1 = \frac{\delta_{1"0"}}{\delta_{1"1"}}; \quad \Delta_2 = \frac{\delta_{2"0"}}{\delta_{2"1"}}. \tag{3}$$

The ratio of the values of the criteria above for the desynchronization mode (transfer log "0") and for the synchronization mode (transfer log "1") determines the value of the noise margin and the possibility to identify logical levels correctly.

3.4 Simulation Results

Confirmation of the presence or absence of synchronization during the transmission of logic levels can be visually assessed by analysing the attractors of the slave oscillators in the presence of interference in the communication line (Fig. 2). When synchronizing (log "1"), the attractor of the slave oscillator (Fig. 2, left) has a strongly pronounced two-loop structure and is concentrated in a limited volume of the phase space. In the mode of desynchronization (log "0"), the attractor starts to fill the phase space evenly and increases its swing (Fig. 2, right).

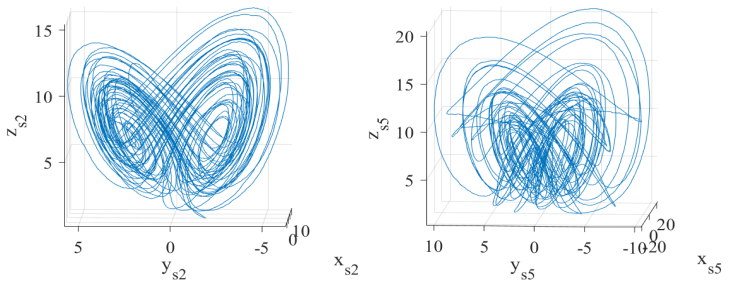

Fig. 2. The attractor of one of the slave oscillators during synchronization (left) and at desynchronization (right) with SNR = 10.

Using the visual criteria (Fig. 2), the most optimal control parameter groups of the slave and master oscillators are identified according to the criteria of maximum similarity in the spectral unevenness, effective value and mutual correlation properties.

The main attention during modelling was given to the possibility of the transmission system operation under conditions of a significant level of interference. In most proposed transmission systems based on chaotic subcarriers, the minimum achievable SNR does not exceed 30–40 dB.

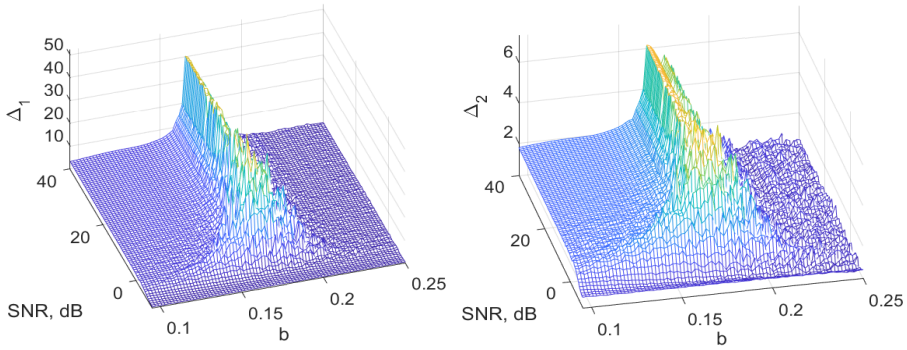

Fig. 3. Dependence of mean square (left) and average rectified (right) deviation on the communication parameter and SNR, dB.

The results of mathematical modelling of the proposed system, the maximization of values by the criterion of mean square δ_1 and average rectified values δ_2 showed the presence of considerable stability of the system to interference. System performance was ensured at SNR level >0 dB, under the condition of values of the coupling parameter of chaotic oscillators 0.13<b<0.18 (Fig. 3). Thus, the possibility of transmitting digital information is confirmed, when interference level in the signal is commensurable with the level of the signal, which allows us to call such a transmission scheme superstable to noise.

4. CONCLUSIONS

A telecommunication system for the transmission of digital signals using the Rucklidge oscillator signals as subcarriers has been proposed in the research. A number of criteria for testing the quality characteristics of the system synchronization under interference conditions have also been proposed in the paper.

The simulation of the proposed data transmission system has been carried out, as a result of which the values of control parameters, communication parameters and interference level have been established, which ensure digital information transmission with the maximum degree of action reliability and concealment.

The use of the advantages of ultra-wideband chaotic signals in a data transmission system based on the implemented synchronization method has the prospect of being used to transmit information in various industries such as electric transport, automobile industry, railway industry etc., which have high noise immunity requirements due to a large number of electromagnetic radiation sources.

ACKNOWLEDGEMENTS

The research leading to these results has been supported by the European Regional Development Fund project "Development of Competence Centre of Mechanical Engineering", contract No.1.2.1.1/16/A/003 signed between the Competence Centre of Mechanical Engineering and Central Finance and Contracting Agency, Research No. 3.2. "Dual Fuel System Development for a Diesel Engine Locomotive".

REFERENCES

1. Andronov, A.A. (1988). To the mathematical theory of capture. *Magazine of Applied Physics*, *7*, 3–11.
2. Koronovsky, A.A. (2009). About the application of chaotic synchronization for the hidden transmission of information. *Uspekhi Fizicheskikh Nauk*, *12*, 1281–1310.
3. Volkovsky, A.R., & Rulkov, N.F. (1993). Synchronous chaotic response of a non-linear information transfer system with a chaotic carrier. *Letters in ZhTF*, *19*(3), 71.
4. Anishchenko, V.S. (1992). Synchronization of chaos. *Int. J. of Bifurcation and Chaos., 2*(3), 633–644.
5. Bellman, R. (1969). *Introduction to matrices theory*. M: The science.
6. Golevich, O.B. (2014). The method of matching chaotic signals to be used in ultrabroadband communication systems. *Measuring and Computing Equipment in Technological Processes*, *3*, 173–175.
7. Golevich, O.B. (2015). Chaotic signals ensembles order and the way to use them in ultrabroadband communication systems. *Digital Technologies*, *17*, 181–191.
8. Pehlivan, İ., Uyaroğlu, Y., & Yoğun, M. (2010). Chaotic oscillator design and realizations of the rucklidge attractor and its synchronization and masking simulations. *Scientific Research and Essays*, *16*, 2210–2219.

NELINEĀRO DINAMISKO SISTĒMU SINHRONIZĀCIJA TROKŠŅU DARBĪBAS APSTĀKĻOS KANĀLĀ

O.Golevych, O.Pyvovar, P.Dumenko

K o p s a v i l k u m s

Ir paveikta dinamiskās sistēmas Rucklidge analīze un noteiktas vērtības vadības parametriem, kas nodrošina digitālās informācijas nodošanu ar maksimālu ticamības pakāpi un darbības slepenību. Balstoties uz izstrādāto sinhronizācijas veidu, ierosināts izveidot digitālo signālu pārraides telekomunikācijas sistēmu, izmantojot ģeneratora Rucklidge signālus.

23.05.2018.